

Energy Budget Constraints on the Time History of Aerosol Forcing and Climate Sensitivity

Chris Smith^{1,1,1}, Glen Harris^{2,2,2}, Matthew Palmer^{2,2,2}, Nicolas Bellouin^{3,3,3}, Gunnar Myhre^{4,4,4}, Michael Schulz^{5,5,5}, Jean-Christophe Golaz^{6,6,6}, Mark Ringer^{2,2,2}, Trude Storelvmo^{7,7,7}, Piers Forster^{1,1,1}, and William Collins^{8,8}

¹University of Leeds

²Met Office Hadley Centre

³University of Reading

⁴CICERO

⁵Norwegian Meteorological Institute

⁶Lawrence Livermore National Laboratory

⁷University of Oslo

⁸University of Reading, University of Reading Department of Meteorology

November 30, 2022

Abstract

An observationally-constrained time series of historical aerosol effective radiative forcing (ERF) from 1750 to 2019 is developed in this paper. We find that the time history of aerosol ERFs diagnosed in CMIP6 models exhibits considerable variation and explore how the time history of aerosol forcing influences the probability distributions of present-day aerosol forcing and emergent metrics such as climate sensitivity. Using a simple energy balance model, trained on CMIP6 climate models and constrained by observed near-surface warming and ocean heat uptake, we derive estimates for the historical aerosol forcing. We find 2005-2014 mean aerosol ERF to be -1.1 (-1.8 to -0.5) W m⁻² relative to 1750. Assuming recently published historical emissions from fossil fuel and industrial sectors and biomass burning emissions from SSP2-4.5, aerosol ERF in 2019 is -0.9 (-1.5 to -0.4) W m⁻². There is a modest recovery in aerosol forcing (+0.025 W m⁻² decade⁻¹) between 1980 and 2014. This analysis also gives a 5-95% range of equilibrium climate sensitivity (ECS) of 1.8-5.1C (best estimate 3.1C) with a transient climate response (TCR) of 1.2-2.6C (best estimate 1.8C).

Energy Budget Constraints on the Time History of Aerosol Forcing and Climate Sensitivity

C. J. Smith^{1,2}, G. R. Harris³, M. D. Palmer³, N. Bellouin⁴, W. Collins⁴, G. Myhre⁵, M. Schulz⁶, J.-C. Golaz⁷, M. Ringer³, T. Storelvmo⁸ and P. M. Forster¹

¹Priestley International Centre for Climate, University of Leeds, UK.

²International Institute for Applied Systems Analysis (IIASA), Laxenburg, Austria.

³Met Office Hadley Centre, Exeter, UK.

⁴Department of Meteorology, University of Reading, UK.

⁵Center for International Climate and Environmental Research in Oslo (CICERO), Norway.

⁶Norwegian Meteorological Institute, Oslo, Norway.

⁷Lawrence Livermore National Laboratory, Livermore, CA, USA.

⁸Department of Geosciences, University of Oslo, Norway.

Corresponding author: Chris Smith (c.j.smith1@leeds.ac.uk)

Key Points:

- We determine the most plausible time history of aerosol forcing that matches surface temperature and Earth energy uptake constraints
- Constrained aerosol forcing shows a modest recovery between 1980 and 2014, slower than the rate simulated by many CMIP6 models
- The best estimate aerosol forcing using this method is -1.10 W m^{-2} for 2005-14 relative to 1750.

24 **Abstract**

25 An observationally-constrained time series of historical aerosol effective radiative forcing (ERF)
26 from 1750 to 2019 is developed in this paper. We find that the time history of aerosol ERFs
27 diagnosed in CMIP6 models exhibits considerable variation and explore how the time history of
28 aerosol forcing influences the probability distributions of present-day aerosol forcing and
29 emergent metrics such as climate sensitivity. Using a simple energy balance model, trained on
30 CMIP6 climate models and constrained by observed near-surface warming and ocean heat
31 uptake, we derive estimates for the historical aerosol forcing. We find 2005-2014 mean aerosol
32 ERF to be -1.1 (-1.8 to -0.5) W m^{-2} relative to 1750. Assuming recently published historical
33 emissions from fossil fuel and industrial sectors and biomass burning emissions from SSP2-4.5,
34 aerosol ERF in 2019 is -0.9 (-1.5 to -0.4) W m^{-2} . There is a modest recovery in aerosol forcing
35 ($+0.025 \text{ W m}^{-2} \text{ decade}^{-1}$) between 1980 and 2014. This analysis also gives a 5-95% range of
36 equilibrium climate sensitivity (ECS) of 1.8 - 5.1°C (best estimate 3.1°C) with a transient climate
37 response (TCR) of 1.2 - 2.6°C (best estimate 1.8°C).

38 **Plain Language Summary**

39 There are two main human drivers of climate change: (i) Greenhouse gas emissions, which warm
40 the planet; and (ii) air pollution (aerosols) that offset some of this warming. Unfortunately,
41 disentangling the effects of historical aerosol cooling is difficult based on the available
42 observations. Therefore, we often use climate models to estimate how much aerosols have
43 cooled the Earth since the start of the Industrial Revolution. Over the mid-to-late 20th Century,
44 some climate models simulate less warming compared to 1850 than has been observed. This may
45 be because aerosol cooling in some climate models is too strong. Our approach combines the
46 relationships between aerosol emissions and their cooling effects on temperature from 11 climate
47 models with simpler representations of the underlying physics. This simpler mathematical
48 framework allows us to more fully account for uncertainty in both the aerosol cooling and its
49 effects on surface temperature and ocean heat uptake by running a much larger set of
50 simulations. Our results suggest that the effect of aerosol cooling has only unwound slowly
51 since 1980, and that it is difficult to determine how sensitive the climate is from this method.

52 **1 Introduction**

53 Aerosol effective radiative forcing remains one of the most uncertain components of the
54 present-day climate (Bellouin, Quaas, et al., 2020). Uncertainty in present-day forcing reduces
55 our ability to confidently predict the future climate response to emissions (Forster et al., 2013)
56 and the level of historical greenhouse gas warming masked by the cooling effect of aerosols
57 (Samset et al., 2018). Aerosol forcing is the largest uncertainty governing future committed
58 warming (Matthews & Zickfeld, 2012; Smith et al., 2019) and remaining carbon budgets
59 consistent with Paris Agreement targets (Mengis & Matthews, 2020). In most future socio-
60 economic scenarios, aerosol forcing is projected to become less negative over the 21st century
61 (Gidden et al., 2019; Huppmann et al., 2018; Rogelj et al., 2018), promoting an increase in the
62 rate of warming unless there is a concurrent reduction in greenhouse gas emissions (Shindell &
63 Smith, 2019). The time history of aerosol ERF is a necessary input to many reduced-complexity
64 climate models (Nicholls et al., 2020), which in turn may be driven by simple emissions-to-
65 forcing based relationships; these simple models find enormous utility when coupled to
66 integrated assessment models (Huppmann et al., 2018).

67 Given its large uncertainty, aerosol forcing has remained an active research area. Several
68 studies have quantified the aerosol effective radiative forcing (ERF) in the present day relative to
69 pre-industrial based on observations, models, energy balance arguments, or a combination of
70 approaches (Andrews & Forster, 2020; Bellouin, Quaas, et al., 2020; Boucher et al., 2013;
71 Fiedler et al., 2019; Forest, 2018; Forest et al., 2002, 2006; Myhre, Shindell, et al., 2013; Skeie et
72 al., 2018; Smith et al., 2020; Zelinka et al., 2014). Fewer studies have attempted to diagnose a
73 time series of historical aerosol forcing. Murphy et al. (2009) used observations of ocean heat
74 uptake, surface temperature and radiative forcing of long-lived greenhouse gases and volcanic
75 eruptions since 1950 to determine the residual forcing, which was mostly attributed to aerosols.
76 Skeie et al. (2011) and Lund et al. (2018) used chemistry-transport models with prescribed
77 meteorology, evaluated at frequent time slice years since pre-industrial, to determine historical
78 aerosol forcing since 1750. Shindell et al. (2013) used timeslices from 1850, 1930, 1980 and
79 2000 in full-complexity climate models to estimate the historical aerosol forcing. The most
80 complete historical aerosol forcing time series, for 1750 to 2011, is given in Annex II (Prather et
81 al., 2013) of the Intergovernmental Panel on Climate Change Working Group 1 Fifth Assessment
82 Report (AR5), which takes in multiple lines of evidence including the Skeie et al. (2011) and
83 Shindell et al. (2013) modelling studies.

84 Our goal is define an aerosol ERF time series from 1750 to 2019 that is consistent with
85 energy balance constraints from observations; effectively to provide an update to AR5 Annex II
86 that takes into account more recent evidence. Here we take a combination of the climate
87 modelling and energy balance approaches. Under the Radiative Forcing (RFMIP) and Aerosol
88 Chemistry (AerChemMIP) Model Intercomparison Projects, historically time-varying aerosol
89 forcing can be diagnosed directly from CMIP6 models. However, in the multi-model mean,
90 CMIP6 model simulations of global-mean surface air temperature (GSAT) are cooler than
91 observations throughout the latter part of the 20th Century before recovering to near-present
92 levels of warming today (Flynn & Mauritsen, 2020). One hypothesis is that aerosol forcing in the
93 20th Century may be too strong in some CMIP6 models, coupled with high transient climate
94 response (TCR) that causes implausibly rapid recent warming in many models (Tokarska et al.,
95 2020). Nevertheless, CMIP6 models remain an important line of evidence in determining
96 historical aerosol forcing. Unlike for greenhouse gases, proxy records for aerosol forcing are
97 sparse before widespread surface radiation measurements became available in the 1950s
98 (Bellouin, Quaas, et al., 2020; Moseid et al., 2020). No global observations of aerosols were
99 available until the satellite era (late 1970s), whereas CMIP6 models provide aerosol forcing
100 estimates from 1850. Therefore, we use CMIP6 model forcing over the industrial era to inform
101 our estimates of historical aerosol ERF, and “correct” for these responses by constraining the
102 forcing estimates to observations of GSAT and Earth energy uptake (EEU).

103 **2 Methods and Data**

104 This section describes how the historical ERF time series are generated and how
105 observational constraints are used with a simple energy-balance climate model to produce a best
106 estimate and range of historical aerosol forcing estimates. A number of historical aerosol forcing
107 time series are investigated. The primary focus of this study is an ensemble of time series
108 generated from a simple relationship of global annual emissions to global annual historical
109 aerosol ERF, using historical aerosol emissions time series and tuning this relationship (which
110 we call a “forcing emulator”) on CMIP6 models where historical aerosol forcing estimates exist.
111 Following the observational constraining we refer to this time series as “CMIP6-constrained”.

112 We also investigate replacing the CMIP6 emissions time series with scaled estimates of
 113 historical aerosol forcing from 11 CMIP6 models and one chemistry-transport model. This
 114 provides a total of 13 different historical aerosol forcing scenarios.

115

116 Throughout this paper, a probabilistic approach is taken, sampling 100,000 historical
 117 forcing timeseries per scenario with the same number of simple climate model configurations.
 118 Uncertainties in the non-aerosol components of historical forcing (greenhouse gases, land-use
 119 change, black carbon deposition on snow, aviation contrail and contrail cirrus, and natural
 120 forcings) are also taken into account. The resulting GSAT and EEU time series from each
 121 ensemble member is compared to the observational constraints and a weighted posterior
 122 distribution produced of historical aerosol ERF.

123 2.1 Aerosol effective radiative forcing timeseries

124 2.1.1 CMIP6 model output

125 We start with 1850 to 2014 (or beyond) transient aerosol ERF derived from 11 GCMs
 126 (Fig. 1; Table 1). Seven models were provided under RFMIP (Pincus et al., 2016), three under
 127 AerChemMIP (Collins et al., 2017) and one used a similar method to AerChemMIP but with
 128 Atmospheric Model Intercomparison Project (AMIP) sea-surface temperatures (SSTs) rather
 129 than model-diagnosed SSTs (Golaz et al., 2019).

130

131 **Table 1:** CMIP6 models providing transient historical aerosol ERF estimates. Runs extended
 132 beyond 2014 in RFMIP experiments followed an SSP2-4.5 forcing pathway.

Model	Long name	Model variants	Modelling protocol	Ensemble members	Time period	References
CanESM5	Canadian Earth System Model, version 5.0.3	r1i1p2f1 r2i1p2f1 r3i1p2f1	RFMIP	3	1850-2100	Swart et al. (2019)
E3SM-1-0	U.S. Department of Energy (DOE) Energy Exascale Earth System Model (E3SMv1)	3 ensemble member pairs (non-ESGF)	AMIP and AMIP with pre-industrial aerosols	3	1870-2014	Golaz et al. (2019)
GFDL-ESM4	Geophysical Fluid Dynamics Laboratory ESM4.1	r1i1p1f1	AerChemMIP	1	1850-2014	Dunne et al. (2020)
GFDL-CM4	Geophysical Fluid Dynamics Laboratory CM4.0	r1i1p1f1 r3i1p1f1	RFMIP	2	1850-2100	Held et al. (2019)
GISS-E2-1-G	Goddard Institute for Space Studies ModelE 2.1-G	r1i1p1f2	RFMIP	1	1850-2100	Kelley et al. (2020)
HadGEM3-GC31-LL	Met Office Hadley Centre Global Coupled Model 3.1	r1i1p1f3 r2i1p1f3 r3i1p1f3	RFMIP	3	1850-2099	Williams et al. (2018)
IPSL-CM6A-LR	Institut Pierre Simon Laplace	r1i1p1f1	RFMIP	1	1850-2100	Boucher et al. (2020)

	Climate Model 6A (low resolution)					
MIROC6	Model for Interdisciplinary Research on Climate, version 6	r1i1p1f1 r2i1p1f1 r3i1p1f1	RFMIP	3	1850-2100	Tatebe et al. (2019)
MRI-ESM2-0	Meteorological Research Institute Earth System Model version 2.0	r1i1p1f1	AerChemMIP	1	1850-2014	Yukimoto et al. (2019)
NorESM2-LM	Norwegian Earth System Model, version 2	r1i1p2f1 r2i1p2f1 r3i1p2f1	RFMIP	3	1850-2100	Seland et al. (2020)
UKESM1-0-LL	UK Earth System Model	r1i1p1f2	AerChemMIP	1	1850-2014	Sellar et al. (2019)

133
134
135
136
137
138
139
140
141
142
143
144
145
146
147

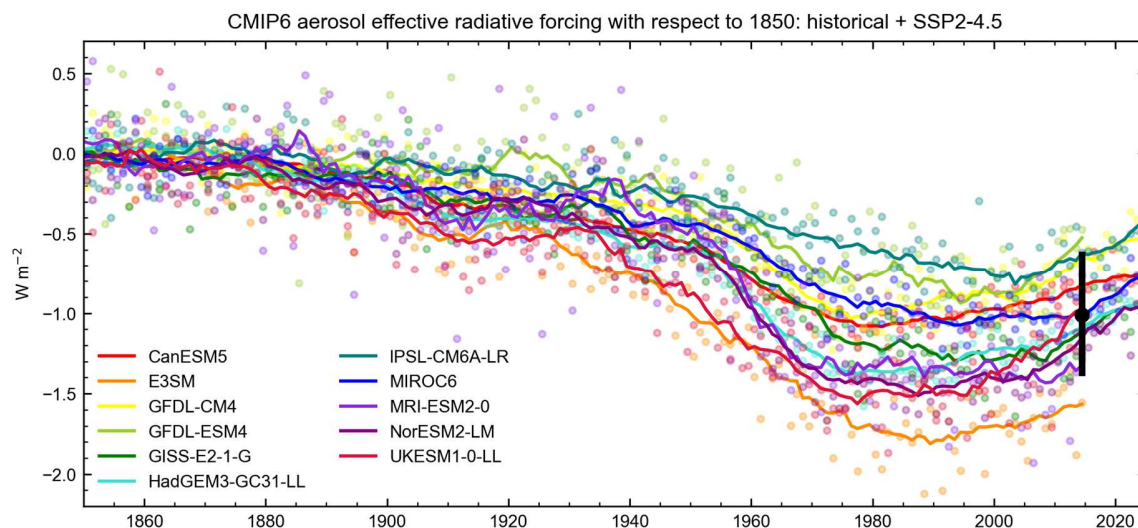
In all cases, aerosol ERF is diagnosed as the top-of-atmosphere radiation flux difference between parallel climate model experiments, one with time-varying aerosols, and one with pre-industrial aerosols (Table 2). In the RFMIP models, SSTs, sea ice and non-aerosol forcings are given as a pre-industrial climatology in both the transient (CMIP6 name piClim-histaer) and control (piClim-control) experiments, with aerosols following the 1850 to 2014 (or 2100, in models running the SSP2-4.5 extension) emissions from CMIP6 in the transient run (Hoesly et al., 2018; van Marle et al., 2017). The pre-industrial control is a 30-year climatology. In AerChemMIP models we use historical (1850-2014) SSTs, sea ice and forcings (histSST) as the perturbation experiment, and historical SSTs, sea-ice and non-aerosol forcings with pre-industrial aerosols (histSST-piAer) as the control. E3SM also followed this method (described in Golaz et al. (2019)).

Table 2: Experiment definitions for the RFMIP and AerChemMIP model runs used in this study.

Protocol	Experiment	Control
RFMIP	CMIP6 name piClim-histaer	CMIP6 name piClim-control
	Pre-industrial SSTs & sea ice	Pre-industrial SSTs and sea ice
	Pre-industrial non-aerosol forcing	Pre-industrial non-aerosol forcing
	Historical aerosol forcing	Pre-industrial aerosol forcing
AerChemMIP	CMIP6 name histSST	CMIP6 name histSST-piAer
	Historical SSTs & sea ice	Historical SSTs & sea ice
	Historical non-aerosol forcing	Historical non-aerosol forcing
	Historical aerosol forcing	Pre-industrial aerosol forcing

148
149
150
151

Figure 1 shows the aerosol effective radiative forcing with respect to 1850 from CMIP6 models. Most models show a peak in negative aerosol forcing at some point between 1975 and 2010 before recovering in recent years.



152
 153 **Figure 1:** CMIP6 diagnosed net aerosol effective radiative forcing relative to an 1850
 154 climatology. Individual years are shown in dots with an 11-year Savitzky-Golay smoothing filter
 155 applied to show solid lines. The black point and line represents the 17-model mean and range
 156 from Smith et al. (2020) for 1850-2014, which did not include E3SM-1-0.
 157

158 2.1.2 Separation of aerosol components

159 For each CMIP6 model, the shortwave (SW) aerosol-radiation and aerosol-cloud
 160 interaction components of the ERF ($ERF_{ari,sw}$ and $ERF_{aci,sw}$) are determined using the
 161 Approximate Partial Radiative Perturbation (APRP) method (Taylor et al., 2007; Zelinka et al.,
 162 2014). The LW ERF from aerosol-cloud interactions ($ERF_{aci,lw}$) was determined using the
 163 difference between all-sky and clear-sky forcing (difference in cloud radiative effect) with the
 164 LW ERF from aerosol-radiation interactions ($ERF_{ari,lw}$) estimated as the difference between
 165 ERF_{lw} and $ERF_{aci,lw}$. The APRP is not exact and a small residual term arises that varies over
 166 time and by model (Fig. S1), some of which is related to a small surface albedo adjustment
 167 (Ghan, 2013), but only the time-varying shapes and relative magnitudes of ERF_{ari} and ERF_{aci} to
 168 each other are important for this decomposition.

169
 170 For the RFMIP models we calculate the APRP using the difference of each year of the
 171 piClim-histaer run against every year of the piClim-control run before averaging across the 30
 172 piClim-control years to determine the ERF_{ari} and ERF_{aci} from each year of 1850 to 2014 (or
 173 2100). This method removes some non-linearities in the APRP (particularly in relation to the
 174 cloud fraction adjustment part of ERF_{aci}) alongside minimising the influence of internal
 175 variability. For the AerChemMIP models and E3SM-1-0, APRP was calculated using the parallel
 176 all-forcing and 1850-aerosol forcing AMIP ensemble members and averaged. In all cases where
 177 modelling groups provided more than one ensemble member, the APRP decomposition is
 178 calculated separately in each ensemble member and then averaged.

179 2.1.3 Forcing emulator

180 Simple emissions-based relationships are then fit to the APRP-derived ERFari and
 181 ERFaci in each CMIP6 model:

$$182 \text{ERFari} = \alpha_{\text{SO}_2} E_{\text{SO}_2} + \alpha_{\text{BC}} E_{\text{BC}} + \alpha_{\text{OC}} E_{\text{OC}} \quad (1)$$

$$184 \text{ERFaci} = -\beta \ln(1 + E_{\text{SO}_2}/s_{\text{SO}_2} + (E_{\text{BC+OC}}/s_{\text{BC+OC}})) \quad (2)$$

185

186 In eqs. (1) and (2), E_{SO_2} , E_{BC} and E_{OC} refer to global annual total emissions in Tg yr⁻¹ of
 187 SO₂, black carbon (BC) and organic carbon (OC), and α_{SO_2} , α_{BC} , α_{OC} , β , s_{SO_2} and $s_{\text{BC+OC}}$ are
 188 scaling coefficients. α values can be interpreted as the radiative efficiency of emission of each
 189 aerosol species. Strictly, eqs. (1) and (2) represent radiative effects rather than radiative forcings.
 190 Radiative forcings are given by the difference of radiative effects in eqs. (1) and (2) calculated
 191 between the emissions in the year of interest and the pre-industrial year (either 1850 or 1750).

192

193 Equation (1) follows from studies showing that ERFari scales linearly with emissions
 194 (Johnson et al., 2019; Lund et al., 2018; Mahajan et al., 2013; Rap et al., 2013). Equation (2) is
 195 an extension of the simple relationship of Stevens (2015) and is based on the understanding that
 196 the change in cloud albedo is logarithmic with sulfate burden, and that burden scales with
 197 emissions (Carslaw et al., 2013; Charlson et al., 1992). Including carbonaceous aerosol in eq. (2)
 198 represented by the sum of BC and OC emissions is useful as some CMIP6 models include the
 199 effects of BC and/or OC on the change in cloud condensation nuclei. The resulting aerosol-cloud
 200 interactions can be substantial, for example a negative ERFaci to BC emissions in the MIROC6
 201 model (Thornhill et al., 2021). Equation (2) is found to give a good heuristic approximation of
 202 global-mean ERFaci to a more sophisticated aerosol indirect effect model (Ghan et al., 2013) as
 203 shown in Smith, Forster, et al. (2018). The sum of BC and OC emissions is used following the
 204 original Ghan et al. (2013) aerosol indirect model which considers primary anthropogenic
 205 emissions to be BC+OC, and to limit the number of free parameters in eq. (2) to three.

206

207 α_{SO_2} , α_{BC} , α_{OC} , β , s_{SO_2} and $s_{\text{BC+OC}}$ parameters in eqs. (1) and (2) are estimated using a
 208 least-squares curve fit of each CMIP6 model's ERFari and ERFaci (Table 3). A multi-model
 209 mean emulation is performed where the ERFari and ERFaci from the 11 models is averaged and
 210 eqs. (1) and (2) applied. The multi-model mean α coefficients (-2.5, +28.5 and -8.5 mW m⁻² (Tg
 211 yr⁻¹)⁻¹ for SO₂, BC and OC respectively) are of similar magnitudes to the radiative efficiencies
 212 from AeroCom models (Myhre, Samset, et al., 2013) for SO₂ and BC, and a little stronger for OC
 213 here. The radiative efficiency coefficients are negative for BC and positive for OC in the IPSL-
 214 CM6A-LR model. However, using coefficients derived from the AerChemMIP single-forcing
 215 experiments for BC, OC and SO₂ in IPSL-CM6A-LR-INCA gives a much less good fit to the
 216 historical aerosol forcing in IPSL-CM6A-LR than our fitted coefficients, and while the fitted
 217 coefficients may not be representative of the true physical behavior in this model, allowing these
 218 values as part of the prior sampling allows for a larger diversity of aerosol forcing time series.
 219 We do not attribute a nitrate forcing to avoid overfitting and because most models do not include
 220 the effects of nitrogen compounds on aerosol formation. In reality, nitrate formation may
 221 compete with sulfate formation for available ammonium. Model evidence suggests this is of
 222 limited importance historically (Thornhill et al., 2021), but may become more important in future
 223 scenarios where the nitrate to sulfate emissions ratio is projected to increase (Bellouin et al.,
 224 2011; Hauglustaine et al., 2014).

225

226

227

228

229

230

231

232

233

234

235

236

237

238

The best-fit values for s_{SO_2} and s_{BC+OC} span several orders of magnitude. We treat these terms as shape parameters, describing how linear or logarithmic the change in ERF_{aci} is with increasing anthropogenic SO_2 and carbonaceous aerosol emissions. With large s_{SO_2} and s_{OC+BC} values, a linear response in ERF_{aci} to emissions is exhibited (from the Taylor expansion of $\ln(1+x) \approx x$ for small x). The degree of logarithmic behaviour that ERF_{aci} exhibits to emissions differs considerably between GCMs (Wilcox et al., 2015) and the possibility that ERF_{aci} may be linear with emissions in some CMIP5 models was discussed in Booth et al. (2018).

Table 3: Forcing emulator coefficients corresponding to eqs. (1) and (2) for each model and the emulation of the multi-model mean forcing. Emissions are in terms of TgSO₂ for α_{SO_2} and TgC for α_{BC} and α_{OC} .

Model	ERF _{ari} (mW m ⁻² (Tg yr ⁻¹) ⁻¹)			ERF _{aci}		
	α_{SO_2}	α_{BC}	α_{OC}	β (W m ⁻²)	s_{SO_2} (TgSO ₂ yr ⁻¹)	s_{BC+OC} (TgC yr ⁻¹)
CanESM5	-2.5	32.6	-0.4	0.727	58.9	24.6
E3SM-1-0	-0.9	24.8	-12.6	2.048	155.9	71.3
GFDL-CM4	-2.6	26.9	-2.1	3.501	692.7	382.9
GFDL-ESM4	-2.6	102	-30.4	3096	913 500	202 620
GISS-E2-1-G	-6.7	146	-44.1	0.563	117.9	16.0
HadGEM3-GC31-LL	-2.9	10.2	1.5	1.004	95.4	77.2
IPSL-CM6A-LR	-0.7	-56.1	8.8	1.097	358.3	518.9
MIROC6	-1.8	38.7	-14.2	0.773	117.2	35.0
MRI-ESM2-0	-3.2	4.5	-10.0	7.404	1276	907.4
NorESM2-LM	-1.5	-18.3	9.7	13 502	1 915 000	944 800
UKESM1-0-LL	-2.4	2.6	0.0	0.741	39.5	228.1
Multi-model mean emulation	-2.5	28.5	-8.5	1.223	156.5	76.7

239

240

241

242

243

244

245

246

247

248

249

250

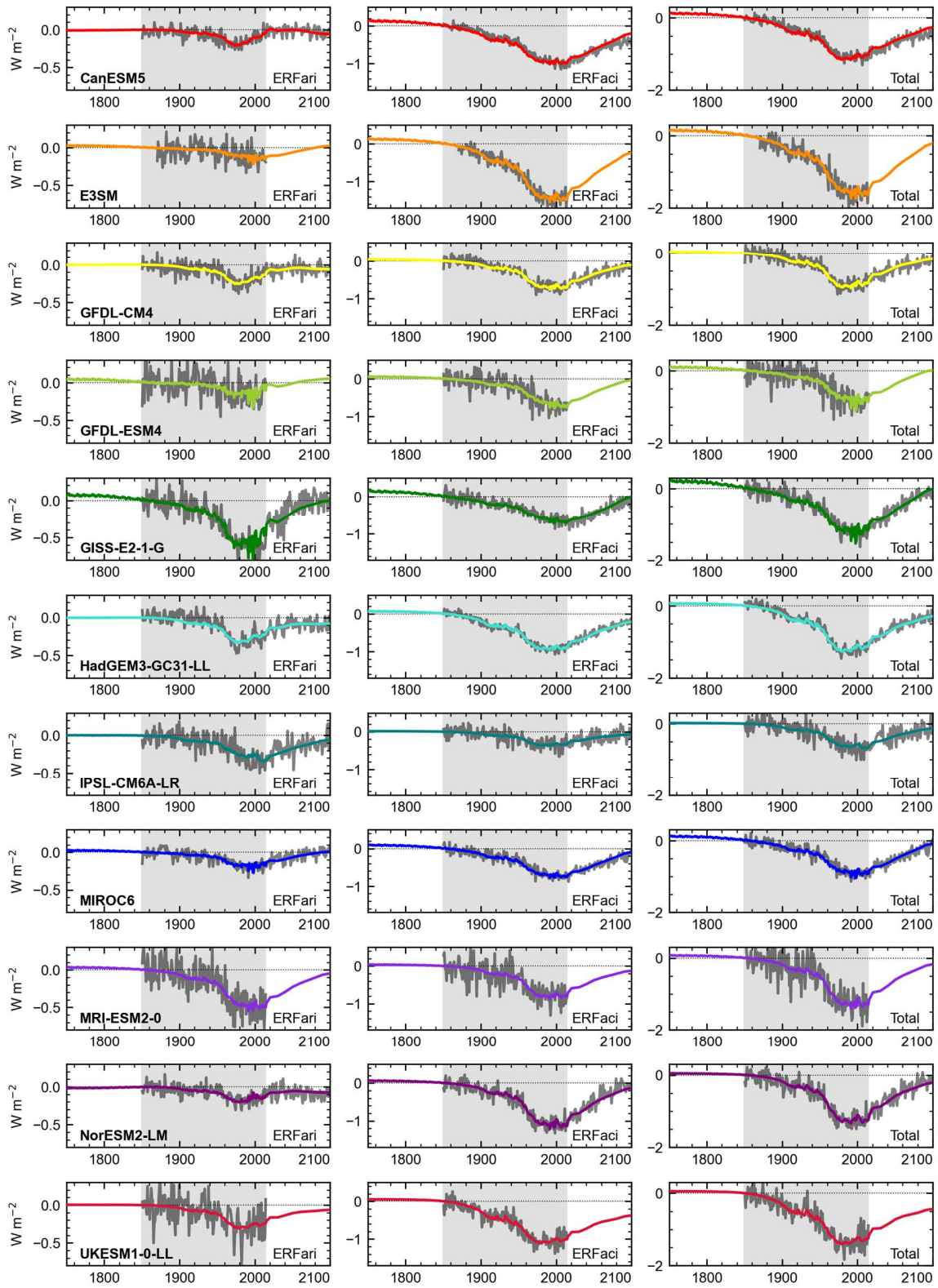
251

252

253

Figure 2 shows the emulated fits to each CMIP6 model from eqs. (1) and (2) as colored curves with the APRP-derived forcing from the GCMs in grey using an 1850 reference. The gray curves in Figure 2 show that most models show a peak in ERF_{ari} that is weakening in recent years, whereas for ERF_{aci} is approximately constant up to 2014 or with a slower weakening trend. It can be seen that the emulated relationships (colored curves) give good representations of each component of the aerosol forcing in each model. We extrapolate these CMIP6 model-specific emulations back to 1750 in each model, resulting in a small positive forcing in 1750 relative to 1850. Where models do not provide an SSP2-4.5 future projection, we also extend these time series forward using eqs. (1) and (2). Finally, we re-base all emulated time series to a 1750 reference (fig. 3), where the impacts of the different shapes for historical aerosol forcing due to different parameter combinations are more clearly seen. One notable feature in all time series is an increased forcing between 2014 and 2015 in the emulated curves owing to a 16% reduction in global SO₂ emissions from the CMIP6 historical to SSP2-4.5 datasets over one year.

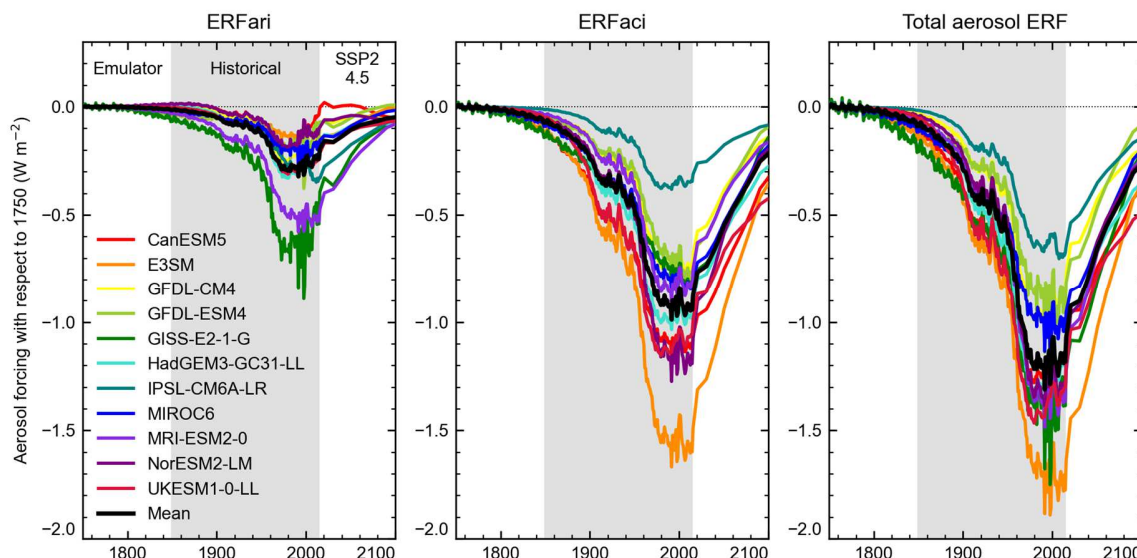
254



255

256 **Figure 2:** simple emissions-based fits from eqs. (1) and (2) to ERFari (left), ERFaci (centre) and
 257 total aerosol forcing (right) for 11 CMIP6 models. Gray curves show the relevant forcing
 258 components from each GCM diagnosed using the APRP method.

259
 260

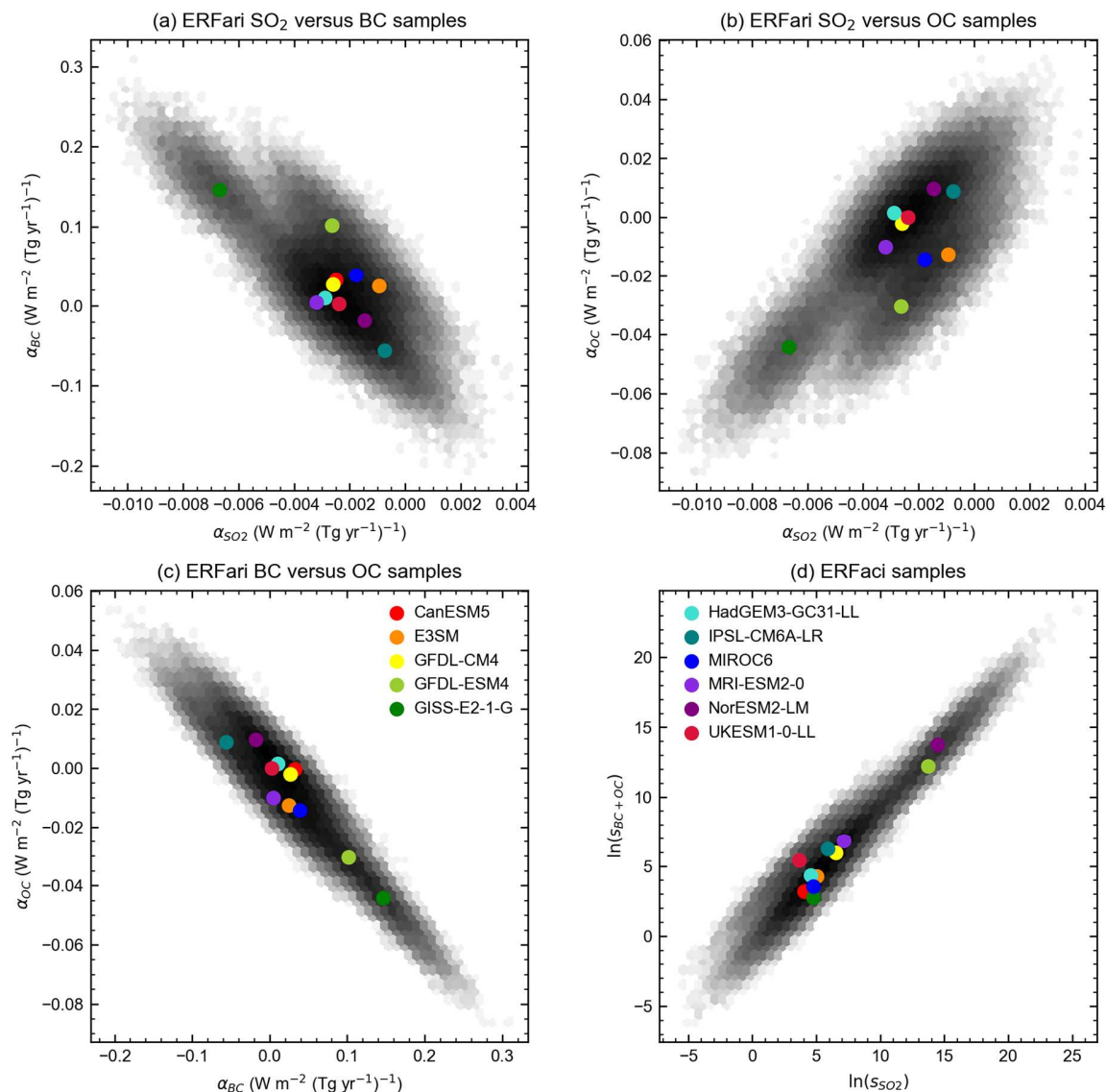


261
 262 **Figure 3:** Emulated emissions to forcing curves, relative to 1750. The multi-model mean
 263 emulation is shown in black.

264 2.1.4 Ensemble generation

265 To simulate time-varying aerosol forcing we take probabilistic ensembles for both the
 266 magnitude and the shape of the historical aerosol forcing. To generate historical shapes, we take
 267 100,000 samples of α_{SO_2} , α_{BC} , α_{OC} , s_{SO_2} and s_{BC+OC} based on their distributions from the 11
 268 participating GCMs (Table 3). A joint kernel-density estimate of the α coefficients is used to
 269 derive a distribution which is then sampled from for ERFari (Fig. 4a-c). Accounting for
 270 correlation between the coefficients maintains the connection that different aerosol species are
 271 often co-emitted. For ERFaci, we take $\ln(s_{SO_2})$ and $\ln(s_{BC+OC})$ from each model and derive a
 272 joint kernel distribution from these two parameters (Fig. 4d). Logarithms of the values in Table 3
 273 are used because the total ERFaci in Eq. (2) has a logarithmic relationship to emissions and
 274 individual model estimates of these parameters span several orders of magnitude. β is not a
 275 degree of freedom in this setup because the resultant ERFaci time series will be scaled as
 276 described below.

277



278
 279 **Figure 4:** Joint distributions of (a) α_{SO_2} and α_{BC} , (b) α_{SO_2} and α_{OC} , (c) α_{BC} and α_{OC} , (d)
 280 $\ln(s_{\text{SO}_2})$ and $\ln(s_{\text{BC}+\text{OC}})$. The grayscale 2D hexbin histogram of points represents a density of
 281 the 100,000 drawn sample sets and the coloured points are fits to each CMIP6 model.

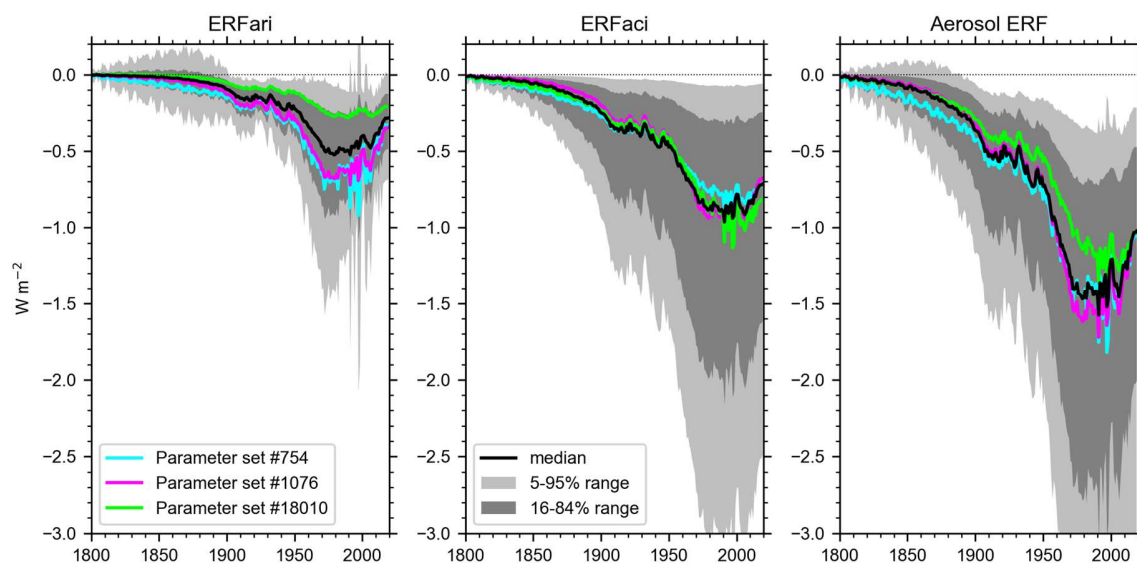
282
 283 We combine the sampled α and s coefficients with 100,000 samples of the absolute
 284 values of the 1850 to 2005-15 ERFari and ERFaci from the process-based assessment in fig. 8 of
 285 Bellouin, Quaas, et al. (2020; hereafter the “Ringberg assessment”), using the distributions that
 286 do not account for energy budget constraints. We run the emissions emulator in eqs. (1) and (2)
 287 using a update of the historical CEDS emissions to 2019 (O’Rourke et al., 2020) for energy and
 288 industrial sectors and BB4CMIP (for biomass burning) under a historical+SSP2-4.5 assumption
 289 (the emissions are much less sensitive to the choice of scenario for biomass burning than for
 290 energy and industry). Critically, the updated CEDS emissions account for phenomena such as an
 291 earlier and more gradual reduction in SO₂ emissions from China than were in the original CMIP6

292 dataset (Paulot et al., 2018), as well as other corrections, and avoids arbitrarily choosing a
 293 scenario for post-2014 emissions. Differences in these time series are plotted in Fig. S2.

294

295 This process rescales the α coefficients and selects β in each ensemble member
 296 consistent with the present-day ERFaci. These 100,000 sampled time series are then rebased to a
 297 1750 baseline by subtracting the 1750 forcing from the 1850 forcing, producing 100,000
 298 candidate historical time series of aerosol forcing for the period 1750-2019 that differ in shape
 299 and magnitude (Fig. 5).

300



301 **Figure 5:** Sampled ERFari, ERFaci and total aerosol ERF time series before constraint.
 302 Overplotted are three individual ensemble members (colored lines) that have present-day total
 303 aerosol forcing close to the ensemble median with different time histories. The 5-95% and 16-
 304 84% ranges of the ensemble are shown as light and dark grey bands with the ensemble median in
 305 black.

307 2.1.5 Scaled model forcing

308

309 Alongside the emissions-based aerosol forcing time series, we repeat the analyses using
 310 scaled historical ERFari and ERFaci from each CMIP6 model, where the shapes of the historical
 311 forcing derived from the APRP method (Fig. 2) in each model are fixed, but the pre-industrial to
 312 present-day magnitudes are allowed to vary. We also use RFari and RFaci time series generated
 313 from the Oslo-CTM3 chemistry transport model (Lund et al., 2018, 2019) for 1750-2020 under
 314 historical+SSP2-4.5. In these 11 CMIP6 models plus Oslo-CTM3, the magnitude of 1850 to
 315 2005-15 forcing is allowed to vary according to the Ringberg assessment distributions, and the
 316 generated time series are extrapolated backwards to a 1750 baseline. Unlike the emissions time
 317 series run with the forcing emulator, the historical shapes of ERFari and ERFaci from these 12
 318 model estimates are fixed.

319 2.2 Non-aerosol forcing time series

320 The non-aerosol component forcings are also generated from a 100,000-member Monte
 321 Carlo ensemble. As they are either less uncertain or smaller in magnitude (or both) than the
 322 aerosol forcing they are not the main focus of this paper but are generated to provide a consistent
 323 view of the total ERF, including uncertainty estimates, so that energy budget constraints can be
 324 applied. Detailed information is provided in Supplementary Text S1 with a summary of the key
 325 data sources in Table 4.

326

327 **Table 4:** Non-aerosol forcing present-day uncertainties and key references.

Forcing type	Description	Key references
Well-mixed greenhouse gases	Concentrations to radiative forcing; tropospheric adjustments	Etminan et al. (2016); Gidden et al. (2019); Hodnebrog, Aamaas, et al. (2020); Hodnebrog, Myhre, et al. (2020); Meinshausen et al. (2017, 2020); Smith et al. (2020); Smith, Kramer, et al. (2018)
Ozone	Analysis of CMIP6 models; precursor emissions to forcing	Skeie et al. (2020); Smith, Forster, et al. (2018); Stevenson et al. (2013)
Other anthropogenic	Land use forcing (including irrigation); black carbon on snow; aviation contrails; stratospheric water vapor from methane oxidation	Bond et al. (2013); Ghimire et al. (2014); Lee et al. (2020); Myhre, Shindell, et al. (2013); Sherwood et al. (2018)
Volcanic	Forcing from stratospheric aerosol optical depth	Global Volcanism Program (2013); Gregory et al. (2016); Kovilakam et al. (2020); Larson & Portmann (2016); Toohey & Sigl (2017)
Solar	Total solar irradiance; tropospheric adjustments	Gray et al. (2009); Matthes et al. (2017); Smith, Kramer, et al. (2018); Vieira et al., (2011)

328

329 2.3 Simple climate model

330 We use our 100,000 member ensemble of aerosol and non-aerosol forcings and run them
 331 in a two-layer energy balance model, including efficacy of deep-ocean heat uptake (Geoffroy,
 332 Saint-Martin, Bellon, et al., 2013; Geoffroy, Saint-Martin, Olivié, et al., 2013; Held et al., 2010).
 333 To perform this many simulations precludes the use of a comprehensive GCM and similar
 334 constrained Monte Carlo ensemble methods using reduced-complexity models have been done
 335 previously (Meinshausen et al., 2009; Smith, Forster, et al., 2018). The structural uncertainty
 336 associated with the choice of simple climate model has been found to have limited impact on
 337 global mean temperature projections in historical simulations (Nicholls et al., 2020). We choose
 338 to use the two-layer model due to its computational efficiency, inclusion of both EEU and
 339 GSAT, and its proven ability as a useful emulator of complex GCMs (Palmer et al., 2018). We
 340 use the formulation from the two Geoffroy et al. papers, hereafter G13a and G13b. The two-layer
 341 model can be written as

342

$$343 C_{\text{mix}} \frac{dT_{\text{mix}}}{dt} = F + \lambda T_{\text{mix}} - \epsilon \gamma (T_{\text{mix}} - T_{\text{deep}}) \quad (3)$$

$$344 \epsilon C_{\text{deep}} \frac{dT_{\text{deep}}}{dt} = \epsilon \gamma (T_{\text{mix}} - T_{\text{deep}}) \quad (4)$$

345

346 where C_{mix} and C_{deep} ($\text{W yr m}^{-2} \text{K}^{-1}$) are the heat capacities of the ocean mixed layer and deep
 347 ocean, T_{mix} and T_{deep} (K) are the respective layer temperature anomalies, λ ($\text{W m}^{-2} \text{K}^{-1}$) is the
 348 climate feedback parameter (using the convention that negative values indicate stabilizing
 349 feedbacks), F (W m^{-2}) is the effective radiative forcing, ε (dimensionless) is the efficacy of deep
 350 ocean heat uptake and γ ($\text{W m}^{-2} \text{K}^{-1}$) the heat transport between the two layers. The relatively
 351 small heat capacity of the land surface and atmosphere compared to the ocean means that it can
 352 be neglected and the GSAT anomaly is given by T_{mix} .

353
 354 All available 44 CMIP6 models that published both abrupt-4xCO2 and piControl
 355 simulations to the Earth System Grid Federation as of 2 July 2020 were used to tune the two-
 356 layer model using the method set out in G13a and G13b. Models that were available on different
 357 resolutions (e.g. NorESM2-LM and NorESM2-MM), and physical and Earth system models
 358 from the same group (e.g. CNRM-CM6-1 and CNRM-ESM2-1) were treated as separate models,
 359 but different physics versions of the same model were not (e.g. r1i1p1f1 and r1i1p3f1 from
 360 GISS-E2-1-G). The two-layer model is tuned to the GSAT and TOA radiation imbalance of each
 361 CMIP6 model's abrupt-4xCO2 run. There are five free parameters in the G13b model: γ , ε , λ ,
 362 C_{mix} and C_{deep} . Radiative forcing from a quadrupling of CO₂ ($F_{4\times}$) is also calibrated using this
 363 method with the abrupt-4xCO2 experiments. Table S1 sets out the parameters for each model
 364 and Fig. S3 shows the temperature evolution in CMIP6 models for the model output and the
 365 simulated two-layer model fits for abrupt-4xCO2. The ECS is an emergent parameter from this
 366 model and is calculated as $F_{4\times}/-2\lambda$. The inclusion of the efficacy of ocean heat uptake in the
 367 two-layer model leads to different and often larger estimates of climate sensitivity than from a
 368 "Gregory regression" of TOA energy imbalance against global mean temperature anomaly for
 369 the first 150 years of abrupt-4xCO2 (the so-called "effective" climate sensitivity, EffCS). The
 370 strengthening of climate feedbacks over time as temperatures approach equilibrium in abrupt-
 371 4xCO2 experiments results in the long-term equilibrium ECS being in the region of 10-30%
 372 larger than EffCS (Rugenstein et al., 2020). The version of the two-layer model that includes
 373 efficacy of ocean heat uptake captures this effect somewhat, and we cautiously refer to our
 374 derived climate sensitivity as ECS for this reason.

375
 376 A joint kernel density estimate distribution of the six input parameters to the two-layer
 377 model are sampled based on the values resulting from the 44 CMIP6 model tunings (marginal
 378 distributions for each parameter are shown in Fig. S4). The joint distribution allows for
 379 correlation between model parameters to be taken into account when sampling (Table S2).

380
 381 Internal variability in GSAT is simulated by analysing the piControl run in all available
 382 models (49 as of 2 July 2020). Global mean temperatures from the piControl simulations are
 383 detrended to remove any residual drift with the residuals around the long term trend taken to be
 384 the internal variability. The autocovariance matrix of these residuals in each model is constructed
 385 by regressing the time series with itself at lag 1 year, lag 2 years, ..., lag n years where n is the
 386 length of the model's piControl simulation. This input is then used as the covariance of a
 387 multivariate Gaussian distribution that governs the time-dependent internal variability of
 388 temperatures in each model. For each ensemble member simulated, one of the 49 CMIP6 models
 389 is selected at random, and 270 years (1750-2019) of internal variability generated based on the
 390 underlying distribution in the selected GCM. This allows for a more realistic construction of
 391 internal variability than a memoryless process noting that in reality events such as ENSO tend to

392 cluster warm and cool years, and also provides for the recreation of low-frequency long-term
 393 internal variability that is present in some models such as CNRM-ESM2-1 (Fig. S5).

394 2.4 Observational constraints

395 We use GSAT estimates from 1850-2019 and total Earth system energy uptake
 396 observations from 1971-2018 to constrain our simulations. To estimate GSAT we use the
 397 Cowtan & Way (2014) dataset of infilled global-mean surface temperatures (GMST; near-
 398 surface temperatures over land and sea-ice and sea-surface temperatures over open ocean) for
 399 1850-2019, multiplied by a time-varying ratio of GSAT/GMST from CMIP5 models under the
 400 historical and RCP8.5 pathways from 1861 to 2014 (Richardson et al., 2016). This ratio
 401 converges towards 1.08 for the recent past (Rogelj et al., 2019) and we extend this ratio forward
 402 to 2019. Both observations and model output are rebased to the 1850-1900 mean as a proxy for
 403 pre-industrial following the IPCC Special Report on 1.5°C. This results in a central estimate of
 404 GSAT warming of 1.10°C for 2010-19 relative to 1850-1900 with a warming trend of 0.30°C per
 405 decade since 2010.

406
 407 For observations of total Earth energy uptake, we use data from the Global Climate
 408 Observing System (GCOS) observational dataset that includes estimates from ocean heat uptake,
 409 cryosphere, atmosphere and land surface (Von Schuckmann et al., 2020). The ocean has
 410 absorbed 89% of the total energy uptake in the Earth system since 1960 owing to its larger
 411 thermal capacity compared to other components of the Earth system. The two-layer model only
 412 tracks heat uptake into the ocean, but to be physically consistent with the total observed EEU we
 413 assume that the heat uptake of the atmosphere, cryosphere and land is taken into account in the
 414 heat uptake of the mixed layer of the ocean. The GCOS dataset extends back to 1960, but we
 415 focus on the period from 1971-2018 due to the limited coverage of deep ocean temperature
 416 observations before the advent of expendable bathythermographs (XBTs) in the late 1960s
 417 (Palmer, 2017). Our constraint is based on the agreement of EEU calculated in the two-layer
 418 model with the total EEU from 1971 to 2018 in GCOS of 358 ± 37 ZJ (1 s.d.).

419
 420 Following the running of the two-layer model, each of the 100,000 ensemble members is
 421 assigned a weight w_i based on how well it reproduces GSAT and EEU observations. The
 422 weighting is based on the model weighting technique of Knutti et al. (2017):

$$423 \quad w_i = \exp\left(-\left(\frac{r_{\text{GSAT},i}^2}{\sigma_{\text{GSAT},D}^2} + \frac{r_{\text{EEU},i}^2}{\sigma_{\text{EEU},D}^2}\right)\right) \quad (5)$$

425
 426 where $r_{X,i}$ is a measure of how well the model reproduces observations for variable X for
 427 ensemble member i , and $\sigma_{X,D}$ is the “radius of model quality” (Sanderson et al., 2015). The
 428 radius of model quality is a subjective choice and for both GSAT and EEU we use assessed
 429 uncertainties. For GSAT, $r_{\text{GSAT},i}$ represents the root-mean-square error (RMSE) of each
 430 ensemble member’s simulated temperature compared to observations and $\sigma_{\text{GSAT},D} = 0.12^\circ\text{C}$ based
 431 on the “likely” (> 66%) range of GMST from the 1850-1900 period to 2006-15 in IPCC Special
 432 Report on Global Warming of 1.5°C. For EEU, we use $r_{\text{EEU},i}$ as the difference in EEU between
 433 the model ensemble member and the GCOS best estimate of 358 ZJ (1971-2018) and use the

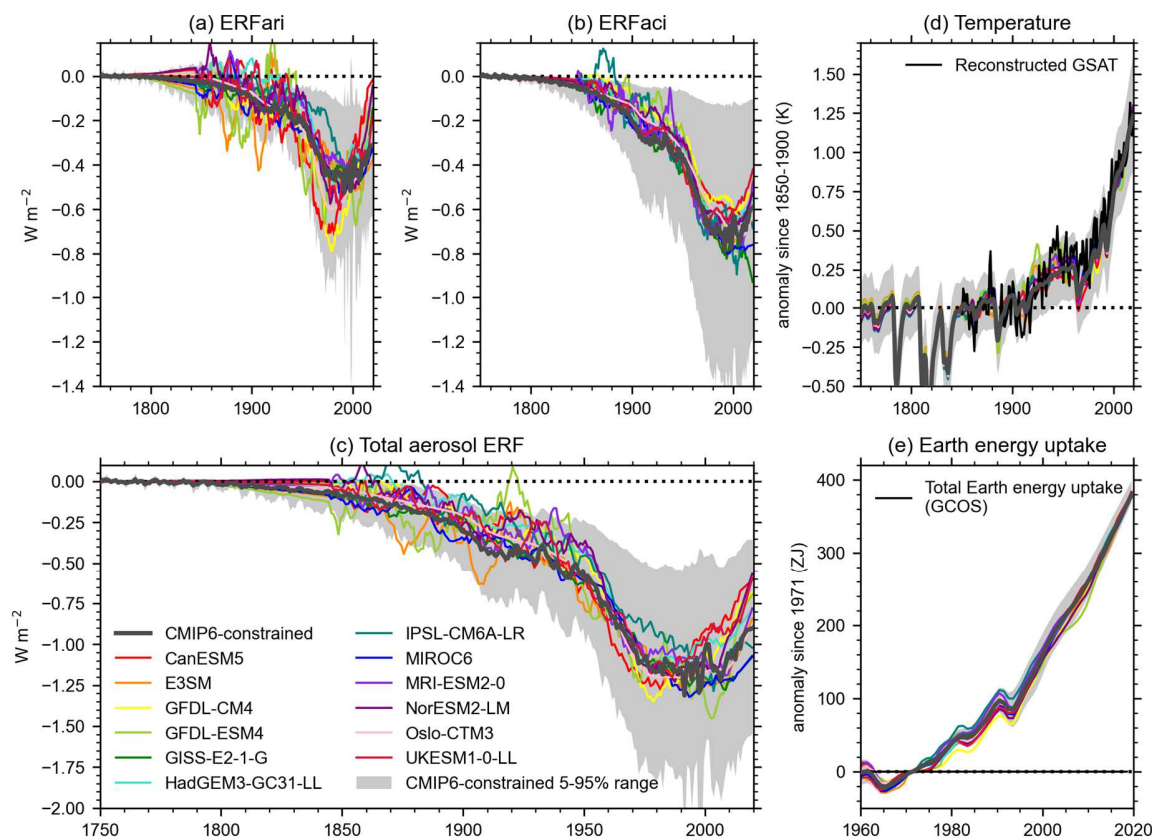
434 GCOS uncertainty of $\sigma_{\text{EEU,D}} = 37 \text{ ZJ}$. Unlike in Knutti et al. (2017) we do not downweight
 435 similar ensemble members.

436
 437 Following calculation of each w_i , the ensemble weights are normalised such that $\sum w_i =$
 438 1. Although subjective, our choices for the goodness-of-fit to the constraints ensure that GSAT
 439 and EEU have approximately equal influence on the total weighting given to each ensemble
 440 member (Fig. S6). An ensemble member will receive a high weight if it is close to both observed
 441 GSAT and observed EEU resulting in fewer high-weight ensemble members than using a single
 442 constraint only. Results using just one constraint are reported in the supplementary material.

443 3 Results

444 Figure 6 shows the aerosol ERF time series that best fit the observational constraints of
 445 GSAT and EEU for the CMIP6-constrained ensemble plus 12 climate models. Also shown are
 446 the projections of GSAT and EEU with the applied ensemble weighting. The weighted 5 to 95%
 447 range from the CMIP6-constrained time series using both GSAT and EEU as constraints is
 448 shown as a grey band with the weighted mean as a grey line. The 1750-2019 aerosol ERF is
 449 determined to be -0.90 W m^{-2} (-1.55 to -0.35 W m^{-2} 5-95% range), comprised from -0.31 (-0.62
 450 to -0.08) W m^{-2} for ERFari and -0.59 (-1.18 to -0.10) W m^{-2} for ERFaci. The central estimate of
 451 total aerosol forcing is equal to the -0.9 (-1.9 to -0.1) W m^{-2} assessed for 1750-2011 in AR5, with
 452 a narrower “very likely” ($> 90\%$) range in this study.

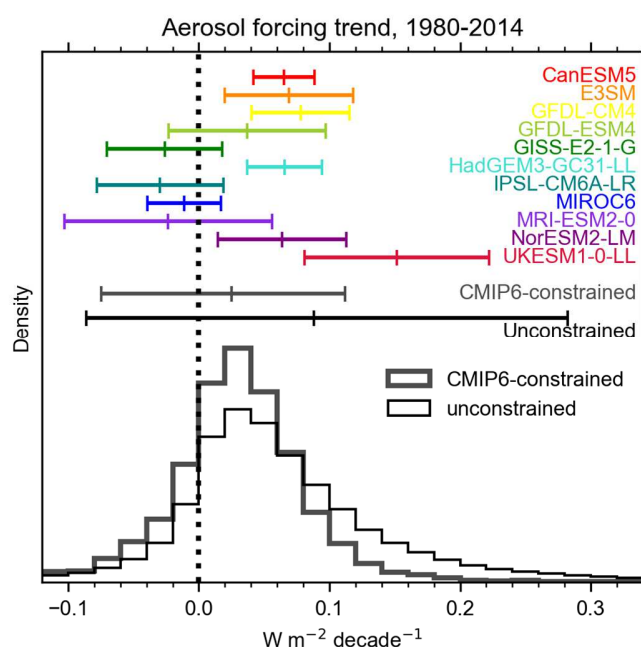
453



454

455 **Figure 6:** Weighted historical time series of (a) ERF_{ari}, (b) ERF_{aci} and (c) total aerosol ERF
 456 time history shapes from each forcing scenario. Curves derived from CMIP6 models and Oslo-
 457 CTM3 are scaled and ensemble-weighted as described in section 2 and do not represent raw
 458 model output. (d) and (e) shows the weighted ensemble simulated global mean surface
 459 temperature and ocean heat uptake. Solid lines are weighted ensemble means and shaded regions
 460 show the weighted 5th-95th percentiles for the CMIP6-constrained time series.

461
 462 With the CMIP6-constrained time series, aerosol ERF exhibits a slight recovery between
 463 1980 and 2014 of $+0.025 \text{ W m}^{-2} \text{ decade}^{-1}$. This is a lower aerosol recovery than seven of the 11
 464 CMIP6 models, although the constrained 5-95% range is wide (-0.074 to $+0.111 \text{ W m}^{-2} \text{ decade}^{-1}$)
 465 and includes the means from all but the UKESM1-0-LL model (Fig. 7). These results indicate
 466 that a rapid aerosol forcing recovery is unlikely and not consistent with the energy budget
 467 constraints, but whether aerosol forcing has been strengthening, weakening or stable in recent
 468 decades is not conclusive.
 469



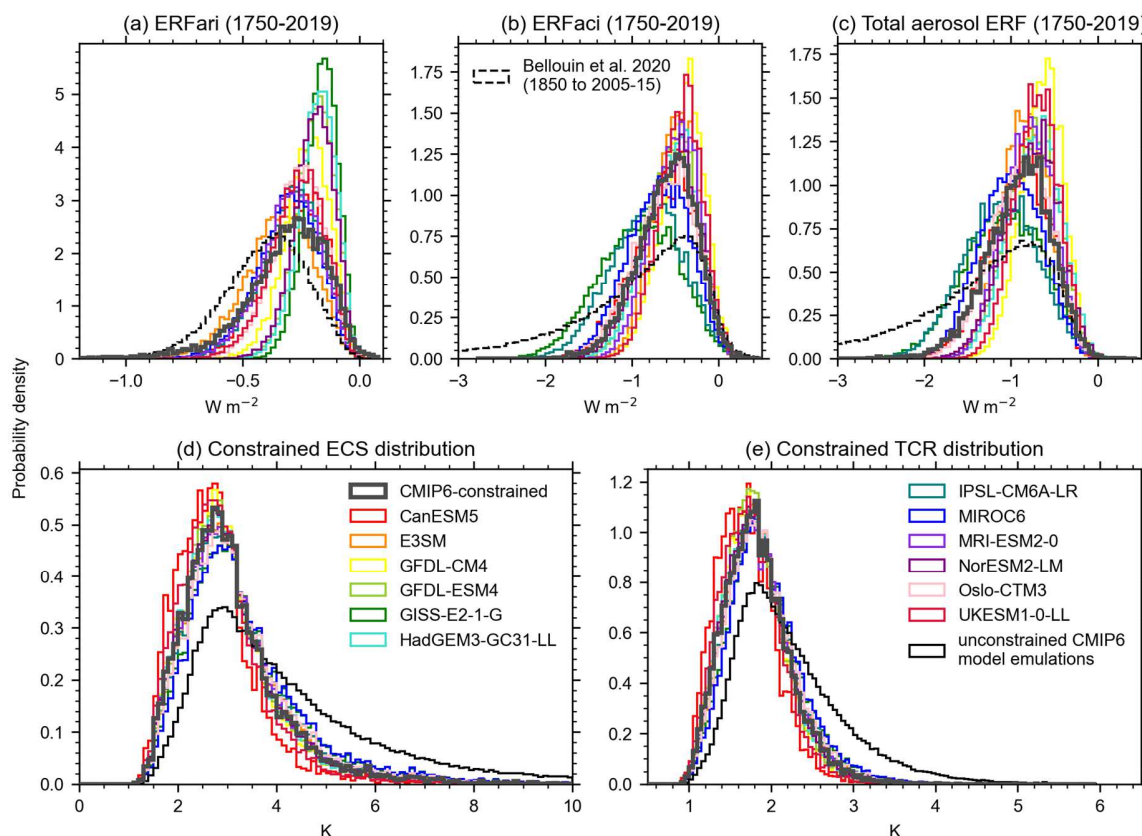
470
 471 **Figure 7:** Histograms of linear aerosol forcing trends for 1980-2014 simulated by the 100,000
 472 member Monte Carlo ensemble (thin black histogram) and weighted after application of
 473 observational constraints in the CMIP6-constrained time series (thick grey histogram). The mean
 474 of these distributions are shown as grey and black lines above the histograms with 5th and 95th
 475 percentiles of the constrained and unconstrained distributions. The trends of each CMIP6
 476 model's aerosol forcing are shown as colored lines, calculated as a 35 year regression from 1980-
 477 2014 and error bars showing 5-95% confidence ranges in the slope of the regression. Numbers
 478 provided in Table S3.

479
 480

481 Figure 8 uses the GSAT and EEU constraints to show the present-day distributions of
 482 aerosol forcing. Alongside this we use the ensemble weights to calculate distributions of ECS

483 and TCR from the ensemble given the two-layer model parameter distributions and ensemble
 484 weights. To calculate TCR we take the approach of Jiménez-de-la-Cuesta & Mauritsen (2019)
 485 noting the TCR is approximately $F_{4\times}/2(-\lambda + \epsilon\gamma)$. The mean, 68% and 90% range for these
 486 parameters along with their unconstrained (prior) distributions are shown in Table 5. All 13
 487 historical time series are shown in Table S4 for both GSAT and EEU constraints, and in Tables
 488 S5 and S6 using only GSAT or EEU respectively.

489
 490 A diversity of constrained present-day aerosol ERF distribution shapes is possible for the
 491 aerosol forcing from each model's historical time evolution. In particular there are a group of
 492 models (the two from GFDL, HadGEM3-GC31-LL, GISS-E2-1-G and NorESM2-LM) where
 493 present-day ERFari is relatively weak and few values less than -0.5 W m^{-2} satisfy the
 494 observational constraints. For ERFaci, neither the CMIP6 models nor the CMIP6-constrained
 495 time series support a strong negative forcing and the constrained distributions are less skewed
 496 than the Ringberg assessment range. All historical aerosol forcing time series constrain the
 497 present-day aerosol forcing to a narrower range than the full process-based distributions of the
 498 Ringberg assessment. As discussed in Bellouin, Quaas, et al. (2020), energy budget constraints
 499 do not favour a present-day aerosol forcing more negative than -2 W m^{-2} , and this is also borne
 500 out by our distributions in Fig. 8c.
 501



502
 503 **Figure 8:** Distributions of (a) ERFari, (b) ERFaci, (c) total aerosol ERF, (d) ECS and (e) TCR.
 504 Thin black curves show the prior distributions for aerosol forcing, ECS and TCR.
 505

High values of ECS and TCR are also constrained out when applying observational constraints (Fig. 8d,e). The prior distributions in thin black curves allow for ECS values much larger than those seen in CMIP6 models as values of net feedback λ sampled in the prior distribution (Fig. S4) can be close to zero. Interestingly, the choice of historical aerosol forcing time series is less important for constraining ECS and TCR than for the present-day aerosol forcing, and in every case the constrained distribution favours lower climate sensitivity than the energy-balance derived prior. The constrained distribution of ECS is not tight (1.8 to 5.1°C 5-95% range with a best estimate of 3.1°C), which is lower than the raw CMIP6 model range inferred from the two-layer model fits (1.9 to 7.1°C; Table S1). The best estimates reported in the main body of the text, Table 4 and Figs. 6 and 7 relate to the weighted mean of the constrained distributions; the median estimates are provided in Supplementary Tables 4-6. Transient climate response falls in the 5-95% range of 1.2 to 2.6°C (best estimate 1.8°C).

Table 5: Ensemble percentiles for aerosol forcing, ECS and TCR, for the CMIP6-informed constrained distributions. End dates of 2010 represent a 2005-14 mean.

	Time period	5%	16%	mean	84%	95%
Total Aerosol ERF (W m ⁻²)	1750-2019	-1.56	-1.26	-0.90	-0.54	-0.35
	1750-2010	-1.78	-1.50	-1.10	-0.70	-0.48
ERFari (W m ⁻²)	1750-2019	-0.62	-0.47	-0.31	-0.15	-0.08
	1750-2010	-0.77	-0.59	-0.40	-0.21	-0.12
ERFaci (W m ⁻²)	1750-2019	-1.18	-0.93	-0.59	-0.26	-0.10
	1750-2010	-1.36	-1.08	-0.69	-0.31	-0.12
ECS (°C)	Constrained	1.76	2.15	3.10	3.94	5.11
TCR (°C)	Constrained	1.24	1.43	1.83	2.22	2.57

4 Discussion and conclusions

Comprehensive climate models are the best tools available for determining global aerosol forcing where other spatially-complete lines of evidence do not exist, such as prior to the satellite era (approximately 1980). However, model-derived aerosol forcing depends on a chain of processes, and ultimately on spatially-resolved aerosol emissions time series that are themselves uncertain (Hoesly et al., 2018). It is not possible to determine here whether the tendency for some models to project strong aerosol forcing in the second half of the 20th Century and/or too much of a recent aerosol recovery, at least compared to what would be implied by the observational constraints, is due to model processes or uncertainties in the emissions.

It is likely that regional effects are significant and aerosols emitted from different source regions affect the global energy balance in different ways which is not captured in a global emissions to forcing relationship (Kretzschmar et al., 2017). Including how global forcing changes to regional aerosol emissions could be an improvement to the forcing emulator, although may be difficult to implement for aerosol-cloud interactions in marine stratocumulus cloud decks which may be thousands of kilometres from the emissions source (Regayre et al., 2014). However, we show for the 11 GCMs that our relationship is trained on, the forcing emulator works well (Fig. 2) and is useful as a first-order global relationship that incorporates sufficient flexibility in its forcing response to emissions.

542
543
544
545
546
547
548
549
550
551
552
553
554
555
556
557
558
559
560
561
562
563
564
565
566
567
568
569
570
571
572
573
574
575
576
577
578
579
580
581
582
583
584
585
586
587

Our results are consistent with the conclusions of previous studies that have attempted to constrain present-day aerosol forcing based on energy balance arguments. We find that very large negative values of pre-industrial to present-day aerosol ERF are inconsistent with observed warming and total Earth system energy gain (Andrews & Forster, 2020; Forest, 2018; Forest et al., 2002, 2006; Skeie et al., 2018; Smith, Forster, et al., 2018). Our best estimate 1750-2019 aerosol forcing of -0.90 W m^{-2} is similar to recent observationally-constrained studies that put aerosol forcing in the -0.8 to -0.9 W m^{-2} range (Andrews & Forster, 2020; Skeie et al., 2018; Smith, Forster, et al., 2018), and the review of 19 inverse estimates in Forest (2018) of -0.77 W m^{-2} . We also find that the most likely shape of recent (1980-2014) aerosol forcing is approximately constant or with a slightly positive trend, which is in line with reanalysis-derived estimates of aerosol R_{Fari} and R_{Faci} (Bellouin, Davies, et al., 2020), and a rapid recovery in aerosol forcing is not likely.

The shape of historical aerosol forcing time series - whether from our simple emulator or provided by a particular CMIP6 model - does not provide a constraint on the overall 1750-2019 aerosol forcing. However, the choice of aerosol forcing dataset used matters less for constraining ECS and TCR than it does for the shape or magnitude of present-day forcing (Fig. 8). It is difficult to constrain the upper bound of ECS due to the heavy tail of the prior distribution, and 95th percentile values of ECS range from 4.3 to 6.0°C depending on the aerosol forcing time series used (Table S4). Other studies also show that these constrained climate sensitivity distributions are sensitive to the priors used (Sherwood et al., 2020). For example, our prior sample space informed by CMIP6 models has very few ensemble members with $\text{ECS} < 1.5^\circ\text{C}$ and $\text{TCR} < 1.0^\circ\text{C}$, both lower bounds of the respective “likely” range in AR5, and it is possible that this area of the distribution is undersampled. Note that we do not perform a full Bayesian analysis in this paper. However, our ECS estimate of 3.1°C (1.8 to 5.1°C) is in line with, although with wider uncertainty, than the Bayesian estimate of 3.2 (2.3 to 4.7°C) in Sherwood et al. (2020), which takes into account several lines of evidence in their assessment.

The two-layer model used in this study includes the efficacy of deep ocean heat uptake, which can partially account for the “pattern effect” (Andrews et al., 2018; Sherwood et al., 2020) in which evolving patterns of sea surface temperature change can influence estimates of climate feedback as warming approaches equilibrium. In the notation of Sherwood et al. (2020) the total effective climate feedback can be written $\lambda - \Delta\lambda$ with $\Delta\lambda$ the contribution from the pattern effect. Across the sample of CMIP6 two-layer model calibrations in this study, the pattern effect $\Delta\lambda$ varies from -0.1 to $+0.6 \text{ W m}^{-2} \text{ K}^{-1}$ (mean $+0.2 \text{ W m}^{-2} \text{ K}^{-1}$) between 1980 and 2050 (assuming SSP2-4.5 forcing), similar to previous studies (e.g. Armour (2017)). This *forced* contribution to the pattern effect arises through the efficacy of deep ocean heat uptake in the two-layer model, and occurs where $\epsilon > 1$ (Geoffroy, Saint-Martin, Bellon, et al., 2013) as it is in the majority of CMIP6 model calibrations. The pattern effect means that historically, the effective climate feedback tends to be slightly weaker than the equilibrium feedback, λ . However, this historical pattern effect is not as large as that determined from observed sea-surface temperatures from AMIP models (Andrews et al., 2018) of about $+0.5 \text{ W m}^{-2} \text{ K}^{-1}$, as the historical pattern effect also includes an *unforced* component that is related to internal variability (Zhou et al., 2021). If we included the unforced component of the pattern effect through a further adjustment to $\Delta\lambda$, it is likely our derived historical aerosol forcing would be weaker. However, applying this historical

588 pattern effect approach to our projections is not straightforward. Calculating $\Delta\lambda$ this way requires
589 a 30-year moving window regression (Andrews et al., 2018), and historical simulations in
590 CMIP6 are provided only to 2014 meaning $\Delta\lambda$ can only be estimated until around 2000. $\Delta\lambda$ is
591 sensitive to volcanic eruptions and aerosol forcing (Gregory et al., 2020), and the historical SST
592 record is only one realisation. We therefore do not take the historical approach, but account for
593 the pattern effect through the sampling of deep ocean heat uptake efficacy, and for internal
594 variability through the temporal autocorrelation of piControl runs.
595

596 Our results suggest that the limited number of CMIP6 models considered here have a
597 stronger aerosol forcing than may have actually occurred during the 20th Century and this effect
598 may be responsible for the modest warming in the CMIP6 ensemble mean over this time period
599 ($0.24 \pm 0.22^\circ\text{C}$ for 1961-90 relative to 1850-1900 in CMIP6 models compared to reconstructed
600 GSAT observations of $0.39 \pm 0.06^\circ\text{C}$ over the same period; Fig. S7). The diagnosis of historical
601 aerosol forcing in more CMIP6 models to confirm or disprove this would be welcomed.
602 Inclusion of uncertainties in historical emissions would be useful to determine whether this is a
603 factor in suppression of warming. Re-running of GCMs with updated emissions inventories
604 could determine how sensitive models are to emissions uncertainties, and the importance of
605 regional effects. The time history of aerosol forcing and its present-day magnitude both constrain
606 key climate system uncertainties such as climate sensitivity and the rate of recent warming
607 (Tanaka & Raddatz, 2011). Reducing uncertainty in both will reduce uncertainty in climate
608 projections.

609 **Acknowledgments and Data**

610 We thank Tim Andrews and Adriana Sima for provision of prototype versions of the
611 HadGEM3-GC3.1-LL and IPSL-CM6A-LR model outputs respectively, and Maria Rugenstein
612 and Dirk Oliv   for helpful discussions. We acknowledge the World Climate Research
613 Programme, which, through its Working Group on Coupled Modelling, coordinated and
614 promoted CMIP6. We thank the climate modeling groups for producing and making available
615 their model output, the Earth System Grid Federation (ESGF) for archiving the data and
616 providing access, and the multiple funding agencies who support CMIP6 and ESGF. C.J.S. was
617 supported by a NERC/IIASA Collaborative Research Fellowship (NE/T009381/1). P.M.F. and
618 G.M. were supported by European Union's Horizon 2020 Research and Innovation Programme
619 under grant agreement no. 820829 (CONSTRAIN). G.H., M.D.P. and M.R. were supported by
620 the Joint UK BEIS/Defra Met Office Hadley Centre Climate Programme (GA01101). W.C.
621 acknowledges funding received from the European Union's Horizon 2020 research and
622 innovation programme under grant agreement No 641816 (CRESCENDO). The Energy Exascale
623 Earth System Model (E3SM) is funded by the U.S. Department of Energy, Office of Science,
624 Office of Biological and Environmental Research. Work at LLNL was performed under the
625 auspices of the U.S. Department of Energy by Lawrence Livermore National Laboratory under
626 contract DE-AC52-07NA27344.
627

628 All code and data used in this paper is available from
629 <https://doi.org/10.5281/zenodo.4624765>. The two layer climate model and the APRP code is part
630 of the *climateforcing* python package (v0.1.0) available from
631 <https://doi.org/10.5281/zenodo.4621059> and <https://pypi.org/project/climateforcing/>. Cowtan &
632 Way temperature observations are available at <https://www->

633 users.york.ac.uk/~kdc3/papers/coverage2013/had4_krig_annual_v2_0_0.txt (accessed 24
634 November 2020). GCOS Earth system energy observations are available from
635 https://doi.org/10.26050/WDCC/GCOS_EHI_EXP. CMIP6 model data used in this paper is
636 available from the Earth System Grid Federation at <https://esgf-node.llnl.gov/search/cmip6/>.
637 Model data from the E3SM AMIP pre-industrial aerosol experiment is available from
638 <https://esgf-node.llnl.gov/projects/e3sm/>. The CEDS emissions data (11 September 2020
639 version) is available from <https://doi.org/10.5281/zenodo.4025316>.

640 **References**

- 641 Andrews, T., & Forster, P. M. (2020). Energy budget constraints on historical radiative forcing.
642 *Nature Climate Change*, *10*(4), 313–316. <https://doi.org/10.1038/s41558-020-0696-1>
- 643 Andrews, T., Gregory, J. M., Paynter, D., Silvers, L. G., Zhou, C., Mauritsen, T., et al. (2018).
644 Accounting for Changing Temperature Patterns Increases Historical Estimates of Climate
645 Sensitivity. *Geophysical Research Letters*, *45*(16), 8490–8499.
646 <https://doi.org/10.1029/2018GL078887>
- 647 Armour, K. C. (2017). Energy budget constraints on climate sensitivity in light of inconstant
648 climate feedbacks. *Nature Climate Change*, *7*(5), 331–335.
649 <https://doi.org/10.1038/nclimate3278>
- 650 Bellouin, N., Rae, J., Jones, A., Johnson, C., Haywood, J., & Boucher, O. (2011). Aerosol
651 forcing in the Climate Model Intercomparison Project (CMIP5) simulations by HadGEM2-
652 ES and the role of ammonium nitrate. *Journal of Geophysical Research Atmospheres*,
653 *116*(20). <https://doi.org/10.1029/2011JD016074>
- 654 Bellouin, N., Quaas, J., Gryspeerdt, E., Kinne, S., Stier, P., Watson-Parris, D., et al. (2020).
655 Bounding Global Aerosol Radiative Forcing of Climate Change. *Reviews of Geophysics*,
656 *58*(1), e2019RG000660. <https://doi.org/10.1029/2019RG000660>
- 657 Bellouin, N., Davies, W., Shine, K. P., Quaas, J., Mülmenstädt, J., Forster, P. M., et al. (2020).
658 Radiative forcing of climate change from the Copernicus reanalysis of atmospheric
659 composition. *Earth System Science Data*, *12*(3), 1649–1677. <https://doi.org/10.5194/essd-12-1649-2020>
- 660
- 661 Bond, T. C., Doherty, S. J., Fahey, D. W., Forster, P. M., Berntsen, T., Deangelo, B. J., et al.
662 (2013). Bounding the role of black carbon in the climate system: A scientific assessment.
663 *Journal of Geophysical Research Atmospheres*, *118*(11), 5380–5552.
664 <https://doi.org/10.1002/jgrd.50171>
- 665 Booth, B. B. B., Harris, G. R., Jones, A., Wilcox, L., Hawcroft, M., & Carslaw, K. S. (2018).
666 Comments on “Rethinking the Lower Bound on Aerosol Radiative Forcing.” *Journal of*
667 *Climate*, *31*(22), 9407–9412. <https://doi.org/10.1175/JCLI-D-17-0369.1>
- 668 Boucher, O., Randall, D., Artaxo, P., Bretherton, C., Feingold, G., Forster, P., et al. (2013).
669 Clouds and Aerosols. In Intergovernmental Panel on Climate Change (Ed.), *Climate*
670 *Change 2013 - The Physical Science Basis* (Vol. 9781107057, pp. 571–658). Cambridge:
671 Cambridge University Press. <https://doi.org/10.1017/CBO9781107415324.016>
- 672 Boucher, O., Servonnat, J., Albright, A. L., Aumont, O., Balkanski, Y., Bastrikov, V., et al.
673 (2020). Presentation and Evaluation of the IPSL-CM6A-LR Climate Model. *Journal of*

- 674 *Advances in Modeling Earth Systems*, 12(7). <https://doi.org/10.1029/2019MS002010>
- 675 Carslaw, K. S., Lee, L. A., Reddington, C. L., Pringle, K. J., Rap, A., Forster, P. M., et al.
676 (2013). Large contribution of natural aerosols to uncertainty in indirect forcing. *Nature*,
677 503(7474), 67–71. <https://doi.org/10.1038/nature12674>
- 678 Charlson, R. J., Schwartz, S. E., Hales, J. M., Cess, R. D., Coakley, J. A., Hansen, J. E., &
679 Hofmann, D. J. (1992). Climate Forcing by Anthropogenic Aerosols. *Science*, 255(5043),
680 423–430. <https://doi.org/10.1126/science.255.5043.423>
- 681 Collins, W. J., Lamarque, J.-F., Schulz, M., Boucher, O., Eyring, V., Hegglin, M. I., et al.
682 (2017). AerChemMIP: quantifying the effects of chemistry and aerosols in CMIP6.
683 *Geoscientific Model Development*, 10(2), 585–607. [https://doi.org/10.5194/gmd-10-585-](https://doi.org/10.5194/gmd-10-585-2017)
684 2017
- 685 Cowtan, K., & Way, R. G. (2014). Coverage bias in the HadCRUT4 temperature series and its
686 impact on recent temperature trends. *Quarterly Journal of the Royal Meteorological*
687 *Society*, 140(683), 1935–1944. <https://doi.org/10.1002/qj.2297>
- 688 Dunne, J. P., Horowitz, L. W., Adcroft, A. J., Ginoux, P., Held, I. M., John, J. G., et al. (2020).
689 The GFDL Earth System Model version 4.1 (GFDL-ESM 4.1): Overall coupled model
690 description and simulation characteristics. *Journal of Advances in Modeling Earth Systems*,
691 *Submitted*, 10.1029/2019MS002015. <https://doi.org/10.1029/2019ms002015>
- 692 Etminan, M., Myhre, G., Highwood, E. J., & Shine, K. P. (2016). Radiative forcing of carbon
693 dioxide, methane, and nitrous oxide: A significant revision of the methane radiative forcing.
694 *Geophysical Research Letters*, 43(24), 12,614–12,623.
695 <https://doi.org/10.1002/2016GL071930>
- 696 Fiedler, S., Kinne, S., Huang, W. T. K., Räisänen, P., O'Donnell, D., Bellouin, N., et al. (2019).
697 Anthropogenic aerosol forcing – insights from multiple estimates from aerosol-climate
698 models with reduced complexity. *Atmospheric Chemistry and Physics*, 19(10), 6821–6841.
699 <https://doi.org/10.5194/acp-19-6821-2019>
- 700 Flynn, C. M., & Mauritsen, T. (2020). On the climate sensitivity and historical warming
701 evolution in recent coupled model ensembles. *Atmospheric Chemistry and Physics*, 20(13),
702 7829–7842. <https://doi.org/10.5194/acp-20-7829-2020>
- 703 Forest, C. E. (2018). Inferred Net Aerosol Forcing Based on Historical Climate Changes: a
704 Review. *Current Climate Change Reports*, 4(1), 11–22. [https://doi.org/10.1007/s40641-](https://doi.org/10.1007/s40641-018-0085-2)
705 018-0085-2
- 706 Forest, C. E., Stone, P. H., Sokolov, A. P., Allen, M. R., & Webster, M. D. (2002). Quantifying
707 uncertainties in climate system properties with the use of recent climate observations.
708 *Science*, 295(5552), 113–117. <https://doi.org/10.1126/science.1064419>
- 709 Forest, C. E., Stone, P. H., & Sokolov, A. P. (2006). Estimated PDFs of climate system
710 properties including natural and anthropogenic forcings. *Geophysical Research Letters*,
711 33(1), n/a-n/a. <https://doi.org/10.1029/2005GL023977>
- 712 Forster, P. M., Andrews, T., Good, P., Gregory, J. M., Jackson, L. S., & Zelinka, M. (2013).
713 Evaluating adjusted forcing and model spread for historical and future scenarios in the
714 CMIP5 generation of climate models. *Journal of Geophysical Research Atmospheres*,

- 715 118(3), 1139–1150. <https://doi.org/10.1002/jgrd.50174>
- 716 Geoffroy, O., Saint-Martin, D., Olivié, D. J. L., Voldoire, A., Bellon, G., & Tytéca, S. (2013).
 717 Transient Climate Response in a Two-Layer Energy-Balance Model. Part I: Analytical
 718 Solution and Parameter Calibration Using CMIP5 AOGCM Experiments. *Journal of*
 719 *Climate*, 26(6), 1841–1857. <https://doi.org/10.1175/JCLI-D-12-00195.1>
- 720 Geoffroy, O., Saint-Martin, D., Bellon, G., Voldoire, A., Olivié, D. J. L., & Tytéca, S. (2013).
 721 Transient Climate Response in a Two-Layer Energy-Balance Model. Part II: Representation
 722 of the Efficacy of Deep-Ocean Heat Uptake and Validation for CMIP5 AOGCMs. *Journal*
 723 *of Climate*, 26(6), 1859–1876. <https://doi.org/10.1175/JCLI-D-12-00196.1>
- 724 Ghan, S. J. (2013). Technical Note: Estimating aerosol effects on cloud radiative forcing.
 725 *Atmospheric Chemistry and Physics*, 13(19), 9971–9974. [https://doi.org/10.5194/acp-13-](https://doi.org/10.5194/acp-13-9971-2013)
 726 [9971-2013](https://doi.org/10.5194/acp-13-9971-2013)
- 727 Ghan, S. J., Smith, S. J., Wang, M., Zhang, K., Pringle, K., Carslaw, K., et al. (2013). A simple
 728 model of global aerosol indirect effects. *Journal of Geophysical Research: Atmospheres*,
 729 118(12), 6688–6707. <https://doi.org/10.1002/jgrd.50567>
- 730 Ghimire, B., Williams, C. A., Masek, J., Gao, F., Wang, Z., Schaaf, C., & He, T. (2014). Global
 731 albedo change and radiative cooling from anthropogenic land cover change, 1700 to 2005
 732 based on MODIS, land use harmonization, radiative kernels, and reanalysis. *Geophysical*
 733 *Research Letters*, 41(24), 9087–9096. <https://doi.org/10.1002/2014GL061671>
- 734 Gidden, M. J., Riahi, K., Smith, S. J., Fujimori, S., Luderer, G., Kriegler, E., et al. (2019). Global
 735 emissions pathways under different socioeconomic scenarios for use in CMIP6: a dataset of
 736 harmonized emissions trajectories through the end of the century. *Geoscientific Model*
 737 *Development*, 12(4), 1443–1475. <https://doi.org/10.5194/gmd-12-1443-2019>
- 738 Global Volcanism Program. (2013). Volcanoes of the World v.4.9.0. Smithsonian Institution.
 739 <https://doi.org/10.5479/si.GVP.VOTW4-2013>
- 740 Golaz, J.-C., Caldwell, P. M., Van Roekel, L. P., Petersen, M. R., Tang, Q., Wolfe, J. D., et al.
 741 (2019). The DOE E3SM Coupled Model Version 1: Overview and Evaluation at Standard
 742 Resolution. *Journal of Advances in Modeling Earth Systems*, 11(7), 2089–2129.
 743 <https://doi.org/10.1029/2018MS001603>
- 744 Gray, L. J., Rumbold, S. T., & Shine, K. P. (2009). Stratospheric Temperature and Radiative
 745 Forcing Response to 11-Year Solar Cycle Changes in Irradiance and Ozone. *Journal of the*
 746 *Atmospheric Sciences*, 66(8), 2402–2417. <https://doi.org/10.1175/2009JAS2866.1>
- 747 Gregory, J. M., Andrews, T., Good, P., Mauritsen, T., & Forster, P. M. (2016). Small global-
 748 mean cooling due to volcanic radiative forcing. *Climate Dynamics*, 47(12), 3979–3991.
 749 <https://doi.org/10.1007/s00382-016-3055-1>
- 750 Gregory, J. M., Andrews, T., Ceppi, P., Mauritsen, T., & Webb, M. J. (2020). How accurately
 751 can the climate sensitivity to CO₂ be estimated from historical climate change? *Climate*
 752 *Dynamics*, 54(1–2), 129–157. <https://doi.org/10.1007/s00382-019-04991-y>
- 753 Hauglustaine, D. A., Balkanski, Y., & Schulz, M. (2014). A global model simulation of present
 754 and future nitrate aerosols and their direct radiative forcing of climate. *Atmospheric*
 755 *Chemistry and Physics*, 14(20), 11031–11063. <https://doi.org/10.5194/acp-14-11031-2014>

- 756 Held, I. M., Winton, M., Takahashi, K., Delworth, T., Zeng, F., & Vallis, G. K. (2010). Probing
 757 the Fast and Slow Components of Global Warming by Returning Abruptly to Preindustrial
 758 Forcing. *Journal of Climate*, 23(9), 2418–2427. <https://doi.org/10.1175/2009JCLI3466.1>
- 759 Held, I. M., Guo, H., Adcroft, A., Dunne, J. P., Horowitz, L. W., Krasting, J., et al. (2019).
 760 Structure and Performance of GFDL’s CM4.0 Climate Model. *Journal of Advances in*
 761 *Modeling Earth Systems*, 11(11), 3691–3727. <https://doi.org/10.1029/2019MS001829>
- 762 Hodnebrog, Ø., Myhre, G., Kramer, R. J., Shine, K. P., Andrews, T., Faluvegi, G., et al. (2020).
 763 The effect of rapid adjustments to halocarbons and N₂O on radiative forcing. *Npj Climate*
 764 *and Atmospheric Science*, 3(1). <https://doi.org/10.1038/s41612-020-00150-x>
- 765 Hodnebrog, Ø., Aamaas, B., Fuglestad, J. S., Marston, G., Myhre, G., Nielsen, C. J., et al.
 766 (2020). Updated Global Warming Potentials and Radiative Efficiencies of Halocarbons and
 767 Other Weak Atmospheric Absorbers. *Reviews of Geophysics*, 58(3).
 768 <https://doi.org/10.1029/2019RG000691>
- 769 Hoesly, R. M., Smith, S. J., Feng, L., Klimont, Z., Janssens-Maenhout, G., Pitkanen, T., et al.
 770 (2018). Historical (1750–2014) anthropogenic emissions of reactive gases and aerosols
 771 from the Community Emissions Data System (CEDS). *Geoscientific Model Development*,
 772 11(1), 369–408. <https://doi.org/10.5194/gmd-11-369-2018>
- 773 Huppmann, D., Rogelj, J., Kriegler, E., Krey, V., & Riahi, K. (2018). A new scenario resource
 774 for integrated 1.5 °C research. *Nature Climate Change*, 8(12), 1027–1030.
 775 <https://doi.org/10.1038/s41558-018-0317-4>
- 776 Jiménez-de-la-Cuesta, D., & Mauritsen, T. (2019). Emergent constraints on Earth’s transient and
 777 equilibrium response to doubled CO₂ from post-1970s global warming. *Nature Geoscience*,
 778 12(11), 902–905. <https://doi.org/10.1038/s41561-019-0463-y>
- 779 Johnson, B. T., Haywood, J. M., & Hawcroft, M. K. (2019). Are Changes in Atmospheric
 780 Circulation Important for Black Carbon Aerosol Impacts on Clouds, Precipitation, and
 781 Radiation? *Journal of Geophysical Research: Atmospheres*, 124(14), 7930–7950.
 782 <https://doi.org/10.1029/2019JD030568>
- 783 Kelley, M., Schmidt, G. A., Nazarenko, L. S., Bauer, S. E., Ruedy, R., Russell, G. L., et al.
 784 (2020). GISS-E2.1: Configurations and Climatology. *Journal of Advances in Modeling*
 785 *Earth Systems*, 12(8). <https://doi.org/10.1029/2019MS002025>
- 786 Knutti, R., Sedláček, J., Sanderson, B. M., Lorenz, R., Fischer, E. M., & Eyring, V. (2017). A
 787 climate model projection weighting scheme accounting for performance and
 788 interdependence. *Geophysical Research Letters*, 44(4), 1909–1918.
 789 <https://doi.org/10.1002/2016GL072012>
- 790 Kovilakam, M., Thomason, L. W., Ernest, N., Rieger, L., Bourassa, A., & Millán, L. (2020). The
 791 Global Space-based Stratospheric Aerosol Climatology (version 2.0): 1979–2018. *Earth*
 792 *System Science Data*, 12(4), 2607–2634. <https://doi.org/10.5194/essd-12-2607-2020>
- 793 Kretzschmar, J., Salzmann, M., Mühlmenstädt, J., Boucher, O., & Quaas, J. (2017). Comment on
 794 “Rethinking the Lower Bound on Aerosol Radiative Forcing.” *Journal of Climate*, 30(16),
 795 6579–6584. <https://doi.org/10.1175/JCLI-D-16-0668.1>
- 796 Larson, E. J. L., & Portmann, R. W. (2016). A temporal kernel method to compute effective

- 797 radiative forcing in CMIP5 transient simulations. *Journal of Climate*, 29(4), 1497–1509.
798 <https://doi.org/10.1175/JCLI-D-15-0577.1>
- 799 Lee, D. S., Fahey, D. W., Skowron, A., Allen, M. R., Burkhardt, U., Chen, Q., et al. (2020). The
800 contribution of global aviation to anthropogenic climate forcing for 2000 to 2018.
801 *Atmospheric Environment*, 244, 117834. <https://doi.org/10.1016/j.atmosenv.2020.117834>
- 802 Lund, M. T., Myhre, G., Haslerud, A. S., Skeie, R. B., Griesfeller, J., Platt, S. M., et al. (2018).
803 Concentrations and radiative forcing of anthropogenic aerosols from 1750 to 2014
804 simulated with the Oslo CTM3 and CEDS emission inventory. *Geoscientific Model
805 Development*, 11(12), 4909–4931. <https://doi.org/10.5194/gmd-11-4909-2018>
- 806 Lund, M. T., Myhre, G., & Samset, B. H. (2019). Anthropogenic aerosol forcing under the
807 Shared Socioeconomic Pathways. *Atmospheric Chemistry and Physics*, 19(22), 13827–
808 13839. <https://doi.org/10.5194/acp-19-13827-2019>
- 809 Mahajan, S., Evans, K. J., Hack, J. J., & Truesdale, J. E. (2013). Linearity of Climate Response
810 to Increases in Black Carbon Aerosols. *Journal of Climate*, 26(20), 8223–8237.
811 <https://doi.org/10.1175/JCLI-D-12-00715.1>
- 812 van Marle, M. J. E., Kloster, S., Magi, B. I., Marlon, J. R., Daniau, A.-L., Field, R. D., et al.
813 (2017). Historic global biomass burning emissions for CMIP6 (BB4CMIP) based on
814 merging satellite observations with proxies and fire models (1750–2015). *Geoscientific
815 Model Development*, 10(9), 3329–3357. <https://doi.org/10.5194/gmd-10-3329-2017>
- 816 Matthes, K., Funke, B., Andersson, M. E., Barnard, L., Beer, J., Charbonneau, P., et al. (2017).
817 Solar forcing for CMIP6 (v3.2). *Geoscientific Model Development*, 10(6), 2247–2302.
818 <https://doi.org/10.5194/gmd-10-2247-2017>
- 819 Matthews, H. D., & Zickfeld, K. (2012). Climate response to zeroed emissions of greenhouse
820 gases and aerosols. *Nature Climate Change*, 2(5), 338–341.
821 <https://doi.org/10.1038/nclimate1424>
- 822 Meinshausen, M., Meinshausen, N., Hare, W., Raper, S. C. B., Frieler, K., Knutti, R., et al.
823 (2009). Greenhouse-gas emission targets for limiting global warming to 2°C. *Nature*,
824 458(7242), 1158–1162. <https://doi.org/10.1038/nature08017>
- 825 Meinshausen, M., Vogel, E., Nauels, A., Lorbacher, K., Meinshausen, N., Etheridge, D. M., et al.
826 (2017). Historical greenhouse gas concentrations for climate modelling (CMIP6).
827 *Geoscientific Model Development*, 10(5), 2057–2116. [https://doi.org/10.5194/gmd-10-2057-
828 2017](https://doi.org/10.5194/gmd-10-2057-2017)
- 829 Meinshausen, M., Nicholls, Z. R. J., Lewis, J., Gidden, M. J., Vogel, E., Freund, M., et al.
830 (2020). The shared socio-economic pathway (SSP) greenhouse gas concentrations and their
831 extensions to 2500. *Geoscientific Model Development*, 13(8), 3571–3605.
832 <https://doi.org/10.5194/gmd-13-3571-2020>
- 833 Mengis, N., & Matthews, H. D. (2020). Non-CO2 forcing changes will likely decrease the
834 remaining carbon budget for 1.5 °C. *Npj Climate and Atmospheric Science*, 3(1), 19.
835 <https://doi.org/10.1038/s41612-020-0123-3>
- 836 Moseid, K. O., Schulz, M., Storelvmo, T., Julsrud, I. R., Olivié, D., Nabat, P., et al. (2020). Bias
837 in CMIP6 models as compared to observed regional dimming and brightening. *Atmospheric*

- 838 *Chemistry and Physics*, 20(24), 16023–16040. <https://doi.org/10.5194/acp-20-16023-2020>
- 839 Murphy, D. M., Solomon, S., Portmann, R. W., Rosenlof, K. H., Forster, P. M., & Wong, T.
840 (2009). An observationally based energy balance for the Earth since 1950. *Journal of*
841 *Geophysical Research*, 114(D17), D17107. <https://doi.org/10.1029/2009JD012105>
- 842 Myhre, G., Shindell, D., Bréon, F.-M., Collins, W., Fuglestedt, J., Huang, J., et al. (2013).
843 Anthropogenic and Natural Radiative Forcing. In Intergovernmental Panel on Climate
844 Change (Ed.), *Climate Change 2013 - The Physical Science Basis* (pp. 659–740).
845 Cambridge: Cambridge University Press. <https://doi.org/10.1017/CBO9781107415324.018>
- 846 Myhre, G., Samset, B. H., Schulz, M., Balkanski, Y., Bauer, S., Bernsten, T. K., et al. (2013).
847 Radiative forcing of the direct aerosol effect from AeroCom Phase II simulations.
848 *Atmospheric Chemistry and Physics*, 13(4), 1853–1877. [https://doi.org/10.5194/acp-13-](https://doi.org/10.5194/acp-13-1853-2013)
849 [1853-2013](https://doi.org/10.5194/acp-13-1853-2013)
- 850 Nicholls, Z. R. J., Meinshausen, M., Lewis, J., Gieseke, R., Dommenges, D., Dorheim, K., et al.
851 (2020). Reduced Complexity Model Intercomparison Project Phase 1: Introduction and
852 evaluation of global-mean temperature response. *Geoscientific Model Development*, 13(11),
853 5175–5190. <https://doi.org/10.5194/gmd-13-5175-2020>
- 854 O'Rourke, P. R., Smith, S. J., McDuffie, E. E., Klimont, Z., Crippa, M., Mott, A., et al. (2020,
855 September). CEDS v_2020_09_11 Pre-Release Emission Data. Zenodo.
856 <https://doi.org/10.5281/zenodo.4025316>
- 857 Palmer, M. D. (2017). Reconciling Estimates of Ocean Heating and Earth's Radiation Budget.
858 *Current Climate Change Reports*, 3(1), 78–86. <https://doi.org/10.1007/s40641-016-0053-7>
- 859 Palmer, M. D., Harris, G. R., & Gregory, J. M. (2018). Extending CMIP5 projections of global
860 mean temperature change and sea level rise due to thermal expansion using a physically-
861 based emulator. *Environmental Research Letters*, 13(8), 084003.
862 <https://doi.org/10.1088/1748-9326/aad2e4>
- 863 Paulot, F., Paynter, D., Ginoux, P., Naik, V., & Horowitz, L. W. (2018). Changes in the aerosol
864 direct radiative forcing from 2001 to 2015: observational constraints and regional
865 mechanisms. *Atmospheric Chemistry and Physics*, 18(17), 13265–13281.
866 <https://doi.org/10.5194/acp-18-13265-2018>
- 867 Pincus, R., Forster, P. M., & Stevens, B. (2016). The Radiative Forcing Model Intercomparison
868 Project (RFMIP): experimental protocol for CMIP6. *Geoscientific Model Development*,
869 9(9), 3447–3460. <https://doi.org/10.5194/gmd-9-3447-2016>
- 870 Prather, M., Flato, G., Friedlingstein, P., Jones, C., Lamarque, J.-F., Liao, H., & Rasch, P.
871 (2013). Climate System Scenario Tables. In Intergovernmental Panel on Climate Change
872 (Ed.), *Climate Change 2013 - The Physical Science Basis* (pp. 1395–1446). Cambridge:
873 Cambridge University Press. <https://doi.org/10.1017/CBO9781107415324.030>
- 874 Rap, A., Scott, C. E., Spracklen, D. V., Bellouin, N., Forster, P. M., Carslaw, K. S., et al. (2013).
875 Natural aerosol direct and indirect radiative effects. *Geophysical Research Letters*, 40(12),
876 3297–3301. <https://doi.org/10.1002/grl.50441>
- 877 Regayre, L. A., Pringle, K. J., Booth, B. B. B., Lee, L. A., Mann, G. W., Browse, J., et al. (2014).
878 Uncertainty in the magnitude of aerosol-cloud radiative forcing over recent decades.

- 879 *Geophysical Research Letters*, 41(24), 9040–9049. <https://doi.org/10.1002/2014GL062029>
- 880 Richardson, M., Cowtan, K., Hawkins, E., & Stolpe, M. B. (2016). Reconciled climate response
881 estimates from climate models and the energy budget of Earth. *Nature Climate Change*,
882 6(10), 931–935. <https://doi.org/10.1038/nclimate3066>
- 883 Rogelj, J., Shindell, D., Jiang, K., Fifita, S., Forster, P., Ginzburg, V., et al. (2018). Mitigation
884 Pathways Compatible with 1.5°C in the Context of Sustainable Development. In V.
885 Masson-Delmotte, P. Zhai, H.-O. Pörtner, D. Roberts, J. Skea, P. R. Shukla, et al. (Eds.),
886 *Global Warming of 1.5°C. An IPCC Special Report on the impacts of global warming of*
887 *1.5°C above pre-industrial levels and related global greenhouse gas emission pathways, in*
888 *the context of strengthening the global response to the threat of climate change.*
- 889 Rogelj, J., Forster, P. M., Kriegler, E., Smith, C. J., & Séférian, R. (2019). Estimating and
890 tracking the remaining carbon budget for stringent climate targets. *Nature*, 571(7765), 335–
891 342. <https://doi.org/10.1038/s41586-019-1368-z>
- 892 Rugenstein, M., Bloch-Johnson, J., Gregory, J., Andrews, T., Mauritsen, T., Li, C., et al. (2020).
893 Equilibrium Climate Sensitivity Estimated by Equilibrating Climate Models. *Geophysical*
894 *Research Letters*, 47(4), e2019GL083898. <https://doi.org/10.1029/2019GL083898>
- 895 Samset, B. H., Sand, M., Smith, C. J., Bauer, S. E., Forster, P. M., Fuglestedt, J. S., et al.
896 (2018). Climate Impacts From a Removal of Anthropogenic Aerosol Emissions.
897 *Geophysical Research Letters*, 45(2), 1020–1029. <https://doi.org/10.1002/2017GL076079>
- 898 Sanderson, B. M., Knutti, R., & Caldwell, P. (2015). A Representative Democracy to Reduce
899 Interdependency in a Multimodel Ensemble. *Journal of Climate*, 28(13), 5171–5194.
900 <https://doi.org/10.1175/JCLI-D-14-00362.1>
- 901 Von Schuckmann, K., Cheng, L., Palmer, M. D., Hansen, J., Tassone, C., Aich, V., et al. (2020).
902 Heat stored in the Earth system: Where does the energy go? *Earth System Science Data*,
903 12(3), 2013–2041. <https://doi.org/10.5194/essd-12-2013-2020>
- 904 Seland, Ø., Bentsen, M., Olivié, D., Toniazzo, T., Gjermundsen, A., Graff, L. S., et al. (2020).
905 Overview of the Norwegian Earth System Model (NorESM2) and key climate response of
906 CMIP6 DECK, historical, and scenario simulations. *Geoscientific Model Development*,
907 13(12), 6165–6200. <https://doi.org/10.5194/gmd-13-6165-2020>
- 908 Sellar, A. A., Jones, C. G., Mulcahy, J. P., Tang, Y., Yool, A., Wiltshire, A., et al. (2019).
909 UKESM1: Description and Evaluation of the U.K. Earth System Model. *Journal of*
910 *Advances in Modeling Earth Systems*, 11(12), 4513–4558.
911 <https://doi.org/10.1029/2019MS001739>
- 912 Sherwood, S., Dixit, V., & Salomez, C. (2018). The global warming potential of near-surface
913 emitted water vapour. *Environmental Research Letters*, 13(10).
914 <https://doi.org/10.1088/1748-9326/aae018>
- 915 Sherwood, S., Webb, M. J., Annan, J. D., Armour, K. C., Forster, P. M., Hargreaves, J. C., et al.
916 (2020). An assessment of Earth’s climate sensitivity using multiple lines of evidence.
917 *Reviews of Geophysics*, n/a(n/a), e2019RG000678. <https://doi.org/10.1029/2019RG000678>
- 918 Shindell, D., & Smith, C. J. (2019). Climate and air-quality benefits of a realistic phase-out of
919 fossil fuels. *Nature*, 573(7774), 408–411. <https://doi.org/10.1038/s41586-019-1554-z>

- 920 Shindell, D., Lamarque, J.-F., Schulz, M., Flanner, M., Jiao, C., Chin, M., et al. (2013). Radiative
 921 forcing in the ACCMIP historical and future climate simulations. *Atmospheric Chemistry
 922 and Physics*, 13(6), 2939–2974. <https://doi.org/10.5194/acp-13-2939-2013>
- 923 Skeie, R. B., Berntsen, T. K., Myhre, G., Tanaka, K., Kvalevåg, M. M., & Hoyle, C. R. (2011).
 924 Anthropogenic radiative forcing time series from pre-industrial times until 2010.
 925 *Atmospheric Chemistry and Physics*, 11(22), 11827–11857. <https://doi.org/10.5194/acp-11-11827-2011>
- 927 Skeie, R. B., Berntsen, T., Aldrin, M., Holden, M., & Myhre, G. (2018). Climate sensitivity
 928 estimates – sensitivity to radiative forcing time series and observational data. *Earth System
 929 Dynamics*, 9(2), 879–894. <https://doi.org/10.5194/esd-9-879-2018>
- 930 Skeie, R. B., Myhre, G., Hodnebrog, Ø., Cameron-Smith, P. J., Deushi, M., Hegglin, M. I., et al.
 931 (2020). Historical total ozone radiative forcing derived from CMIP6 simulations. *Npj
 932 Climate and Atmospheric Science*, 3(1). <https://doi.org/10.1038/s41612-020-00131-0>
- 933 Smith, C. J., Forster, P. M., Allen, M., Leach, N., Millar, R. J., Passerello, G. A., & Regayre, L.
 934 A. (2018). FAIR v1.3: a simple emissions-based impulse response and carbon cycle model.
 935 *Geoscientific Model Development*, 11(6), 2273–2297. <https://doi.org/10.5194/gmd-11-2273-2018>
- 937 Smith, C. J., Kramer, R. J., Myhre, G., Forster, P. M., Soden, B. J., Andrews, T., et al. (2018).
 938 Understanding Rapid Adjustments to Diverse Forcing Agents. *Geophysical Research
 939 Letters*, 45(21), 12,023–12,031. <https://doi.org/10.1029/2018GL079826>
- 940 Smith, C. J., Forster, P. M., Allen, M., Fuglestvedt, J., Millar, R. J., Rogelj, J., & Zickfeld, K.
 941 (2019). Current fossil fuel infrastructure does not yet commit us to 1.5 °C warming. *Nature
 942 Communications*, 10(1), 101. <https://doi.org/10.1038/s41467-018-07999-w>
- 943 Smith, C. J., Kramer, R. J., Myhre, G., Alterskjær, K., Collins, W., Sima, A., et al. (2020).
 944 Effective radiative forcing and adjustments in CMIP6 models. *Atmospheric Chemistry and
 945 Physics*, 20(16), 9591–9618. <https://doi.org/10.5194/acp-20-9591-2020>
- 946 Stevens, B. (2015). Rethinking the Lower Bound on Aerosol Radiative Forcing. *Journal of
 947 Climate*, 28(12), 4794–4819. <https://doi.org/10.1175/JCLI-D-14-00656.1>
- 948 Stevenson, D. S., Young, P. J., Naik, V., Lamarque, J.-F., Shindell, D. T., Voulgarakis, A., et al.
 949 (2013). Tropospheric ozone changes, radiative forcing and attribution to emissions in the
 950 Atmospheric Chemistry and Climate Model Intercomparison Project (ACCMIP).
 951 *Atmospheric Chemistry and Physics*, 13(6), 3063–3085. <https://doi.org/10.5194/acp-13-3063-2013>
- 953 Swart, N. C., Cole, J. N. S., Kharin, V. V., Lazare, M., Scinocca, J. F., Gillett, N. P., et al. (2019).
 954 The Canadian Earth System Model version 5 (CanESM5.0.3). *Geoscientific Model
 955 Development*, 12(11), 4823–4873. <https://doi.org/10.5194/gmd-12-4823-2019>
- 956 Tanaka, K., & Raddatz, T. (2011). Correlation between climate sensitivity and aerosol forcing
 957 and its implication for the “climate trap.” *Climatic Change*, 109(3–4), 815–825.
 958 <https://doi.org/10.1007/s10584-011-0323-2>
- 959 Tatebe, H., Ogura, T., Nitta, T., Komuro, Y., Ogochi, K., Takemura, T., et al. (2019).
 960 Description and basic evaluation of simulated mean state, internal variability, and climate

- 961 sensitivity in MIROC6. *Geoscientific Model Development*, 12(7), 2727–2765.
962 <https://doi.org/10.5194/gmd-12-2727-2019>
- 963 Taylor, K. E., Crucifix, M., Braconnot, P., Hewitt, C. D., Doutriaux, C., Broccoli, A. J., et al.
964 (2007). Estimating Shortwave Radiative Forcing and Response in Climate Models. *Journal*
965 *of Climate*, 20(11), 2530–2543. <https://doi.org/10.1175/JCLI4143.1>
- 966 Thornhill, G. D., Collins, W. J., Kramer, R. J., Olivié, D., Skeie, R. B., O'Connor, F. M., et al.
967 (2021). Effective radiative forcing from emissions of reactive gases and aerosols – a multi-
968 model comparison. *Atmospheric Chemistry and Physics*, 21(2), 853–874.
969 <https://doi.org/10.5194/acp-21-853-2021>
- 970 Tokarska, K. B., Stolpe, M. B., Sippel, S., Fischer, E. M., Smith, C. J., Lehner, F., & Knutti, R.
971 (2020). Past warming trend constrains future warming in CMIP6 models. *Science Advances*,
972 6(12), eaaz9549. <https://doi.org/10.1126/sciadv.aaz9549>
- 973 Toohey, M., & Sigl, M. (2017). Volcanic stratospheric sulfur injections and aerosol optical depth
974 from 500 BCE to 1900 CE. *Earth System Science Data*, 9(2), 809–831.
975 <https://doi.org/10.5194/essd-9-809-2017>
- 976 Vieira, L. E. A., Solanki, S. K., Krivova, N. A., & Usoskin, I. (2011). Evolution of the solar
977 irradiance during the Holocene. *Astronomy & Astrophysics*, 531, A6.
978 <https://doi.org/10.1051/0004-6361/201015843>
- 979 Wilcox, L. J., Highwood, E. J., Booth, B. B. B., & Carslaw, K. S. (2015). Quantifying sources of
980 inter-model diversity in the cloud albedo effect. *Geophysical Research Letters*, 42(5), 1568–
981 1575. <https://doi.org/10.1002/2015GL063301>
- 982 Williams, K. D., Copsey, D., Blockley, E. W., Bodas-Salcedo, A., Calvert, D., Comer, R., et al.
983 (2018). The Met Office Global Coupled Model 3.0 and 3.1 (GC3.0 and GC3.1)
984 Configurations. *Journal of Advances in Modeling Earth Systems*, 10(2), 357–380.
985 <https://doi.org/10.1002/2017MS001115>
- 986 Yukimoto, S., Kawai, H., Koshiro, T., Oshima, N., Yoshida, K., Urakawa, S., et al. (2019). The
987 meteorological research institute Earth system model version 2.0, MRI-ESM2.0:
988 Description and basic evaluation of the physical component. *Journal of the Meteorological*
989 *Society of Japan*. <https://doi.org/10.2151/jmsj.2019-051>
- 990 Zelinka, M. D., Andrews, T., Forster, P. M., & Taylor, K. E. (2014). Quantifying components of
991 aerosol-cloud-radiation interactions in climate models. *Journal of Geophysical Research:*
992 *Atmospheres*, 119(12), 7599–7615. <https://doi.org/10.1002/2014JD021710>
- 993 Zhou, C., Zelinka, M. D., Dessler, A. E., & Wang, M. (2021). Greater committed warming after
994 accounting for the pattern effect. *Nature Climate Change*, 11(2), 132–136.
995 <https://doi.org/10.1038/s41558-020-00955-x>

Energy Budget Constraints on the Time History of Aerosol Forcing and Climate Sensitivity

C. J. Smith^{1,2}, G. R. Harris³, M. D. Palmer³, N. Bellouin⁴, W. Collins⁴, G. Myhre⁵, M. Schulz⁶, J.-C. Golaz⁷, M. Ringer³, T. Storelvmo⁸ and P. M. Forster¹

¹Priestley International Centre for Climate, University of Leeds, UK. ²International Institute for Applied Systems Analysis (IIASA), Laxenburg, Austria. ³Met Office Hadley Centre, Exeter, UK. ⁴Department of Meteorology, University of Reading, UK. ⁵Center for International Climate and Environmental Research in Oslo (CICERO), Norway. ⁶Norwegian Meteorological Institute, Oslo, Norway. ⁷Lawrence Livermore National Laboratory, Livermore, CA, USA. ⁸Department of Geosciences, University of Oslo, Norway.

Contents of this file

Text S1
Figures S1 to S8
Tables S1 to S5

Text S1. Non-aerosol radiative forcing timeseries

This supplementary text describes the non-aerosol forcing time series used in the simulations. Most forcing categories are similar to those used in version 1.3 of the Finite-amplitude Impulse Response model (FaIR; Smith, Forster, et al., 2018) with updates where appropriate. Where uncertainty ranges are given, they are taken to be 90% confidence intervals on the 1750-2019 forcing.

Greenhouse gases

Greenhouse gas (GHG) forcings are calculated from concentration to radiative forcing (RF) relationships (Etminan et al., 2016; Hodnebrog, Aamaas, et al., 2020). The re-fitting of the original Oslo line-by-line radiative transfer model results for RF from CO₂, CH₄ and N₂O (Etminan et al., 2016) as implemented by Meinshausen et al. (2020) are used, which reduces the relative error in the fits. GHG concentrations are taken from the observationally-based CMIP6 historical time series for 1750-2014 (Meinshausen et al., 2017) extended forwards to 2020 using the SSP2-4.5 pathway (Gidden et al., 2019). To move from RF to ERF, 5% is added to the RF for CO₂ and 14% subtracted from CH₄ to account for land-surface warming and tropospheric adjustments respectively (Smith, Kramer, et al., 2018). Tropospheric adjustments also account for an additional 7% for N₂O, 13% for CFC-11 and 12% for CFC-12 (Hodnebrog, Myhre, et al., 2020). For all

other GHGs, ERF is assumed to be the same as RF. We apply a $\pm 20\%$ relative uncertainty (5-95% range) on the present-day ERF from CO₂, N₂O and other GHGs except CH₄ for which we apply $\pm 28\%$; this follows AR5 (Myhre et al., 2013b) with an increase in the uncertainty for CH₄ following Etminan et al. (2016). CMIP6 model results suggest these ranges are conservative and the ERF spread is possibly lower (Smith et al., 2020). We do not modify the shape of the historical greenhouse gas forcing as historical concentrations are known with low uncertainty.

Ozone

Historical tropospheric and stratospheric ozone forcing is used from the subset of CMIP6 models in Skeie et al. (2020) that (i) include full tropospheric chemistry; (ii) are not too structurally similar to other models and (iii) produce sensible pre-industrial to present-day ozone forcing estimates (hence UKESM1-0-LL is excluded due to its implausible negative present-day forcing). The full list of retained models from Skeie et al. (2020) is BCC-ESM1-0, CESM2(WACCM6), GFDL-ESM4, GISS-E2-1-H, MRI-ESM2-0 and Oslo-CTM3. For extrapolating tropospheric ozone ERF back before 1850 and forward after 2014, we use CMIP6 historical and SSP2-4.5 precursor emissions to forcing relationships for CO, NO_x, non-methane volatile organic compounds and concentrations of CH₄ from Smith, Forster, et al. (2018), based on Stevenson et al. (2013), and re-fit these coefficients to correspond to the CMIP6 emissions and Skeie et al. (2020) forcing. We use a $\pm 50\%$ uncertainty on the best estimate of tropospheric ozone ERF of $+0.41 \text{ W m}^{-2}$ for 1750-2019. Stratospheric ozone forcing follows the same method, for which the Skeie et al. (2020) model results show that stratospheric ozone depletion from halogenated gases is outweighed by ozone formation from short-lived climate forcers. Stratospheric ozone has a best estimate 1750-2019 ERF of $+0.07 \text{ W m}^{-2}$ to which we apply a $\pm 200\%$ relative uncertainty.

Other anthropogenic forcings

Land use forcing of -0.20 W m^{-2} from 1750-2019 is used as our best estimate, using land-use-derived albedo change from Ghimire et al. (2014) of -0.15 W m^{-2} with irrigation effects on formation of low-level clouds assumed to contribute an additional -0.05 W m^{-2} (Sherwood et al., 2018). To this total land-use forcing we apply a $\pm 75\%$ relative uncertainty. For aviation contrail and contrail-induced cirrus forcing, we use the recent comprehensive assessment of Lee et al. (2020) of 0.0574 (0.019 to 0.098) W m^{-2} for 1750-2018, and extrapolated this forward one year using aviation NO_x projections from SSP2-4.5. Black carbon on snow forcing follows BC emissions in the SSP-historical and SSP2-4.5 time series and is scaled to 0.08 W m^{-2} in 2019 relative to 1750, which is the AR5 best estimate doubled to take into account the forcing efficacy of black carbon on snow assessed as being greater than unity (Bond et al., 2013). The lognormal distribution for the uncertainty range of 0.04 to 0.18 W m^{-2} is applied following AR5 (Myhre et al., 2013a). Stratospheric water vapor from methane oxidation is assumed to have a 1750-2019 best estimate forcing of 0.05 W m^{-2} with a $\pm 100\%$ relative uncertainty.

Volcanic forcing

Volcanic ERF is calculated using -20τ from CMIP5 models (Larson & Portmann, 2016) and an analysis of seven CMIP6 models that provided the piClim-histnat (natural forcings

only) experiment (Fig. S8), where τ is the stratospheric aerosol optical depth (SAOD) at 550 nm. From the CMIP6 models, an estimate of the solar forcing (see below) was subtracted from the total natural forcing to estimate the volcanic forcing. We combine 3 overlapping datasets for SAOD: the eVolv database for the period 500 BCE to 1900 CE (Toohey & Sigl, 2017), the CMIP6 historical volcanic SAOD for 1850-2014, and the GloSSAC dataset for 1979-2018 (Kovilakam et al., 2020). The GloSSAC dataset is converted from SAOD at 525 nm to the target 550 nm using an Ångström exponent of -2.33 (Kovilakam et al., 2020). For 2019 we repeat 2018 noting no significant eruptions occurred (Global Volcanism Program, 2013). A linear transition between eVolv and CMIP6 is performed for 1850-1900 and for CMIP6 to GloSSAC for 1979-1989. The time-mean SAOD over the 2519 years of available data is defined to be the zero forcing, such that quiescent years have a small positive forcing. The rationale for this is that the long-term mean temperature anomaly should be zero when only volcanic forcing is present. Following AR5 analysis of recent eruptions, volcanic ERF is given an uncertainty range of $\pm 50\%$.

Solar forcing

The solar forcing is taken from the derived SATIRE-M ^{14}C solar irradiance database for the 9000 years up to 2014 (Vieira et al., 2011) and the concurrent CMIP6 total solar irradiance from 2015 onwards (Matthes et al., 2017). The solar irradiance timeseries is referenced to the two solar cycles spanning 1745-1765, as a proxy for 1750 conditions. Effective radiative forcing from solar variability is then calculated from the annual total solar irradiance anomaly, multiplied by $\frac{1}{4}$ (geometric effect) $\times 0.71$ (planetary co-albedo) $\times 0.72$ (tropospheric and stratospheric adjustments (Gray et al., 2009; Smith, Kramer, et al., 2018)). To project uncertainty in the solar forcing time series, we vary both the amplitude of the solar magnitude fluctuations ($\pm 50\%$) and the overall solar forcing trend from 1750 to 2019 ($0.0 \pm 0.1 \text{ W m}^{-2}$ as a linear trend).

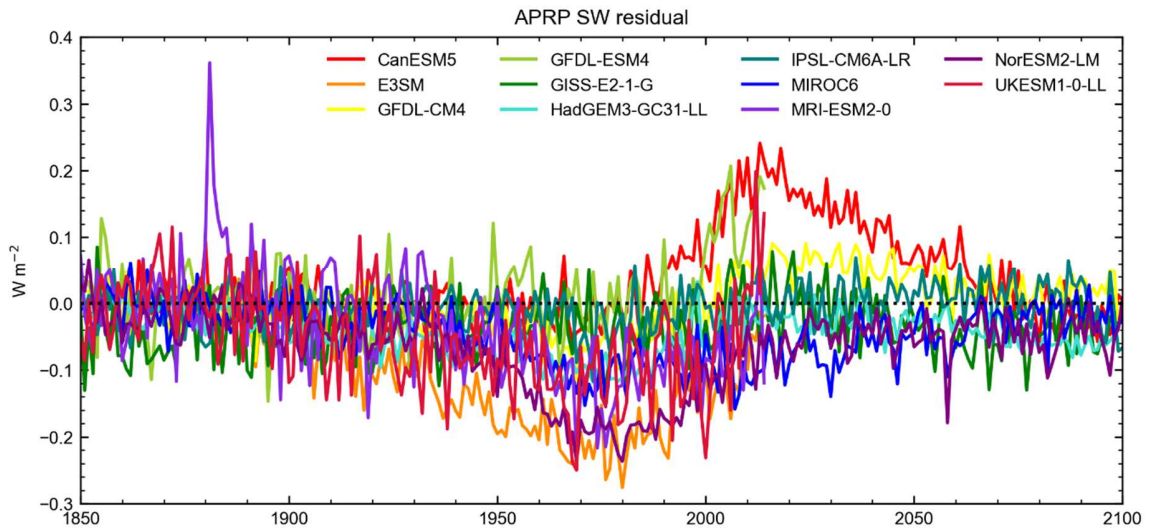


Figure S1: Residual from shortwave APRP decomposition of aerosol ERF in RFMIP and AerChemMIP models and E3SM (showing $ERF_{sw} - ERF_{aer,sw} - ERF_{fac,sw}$)

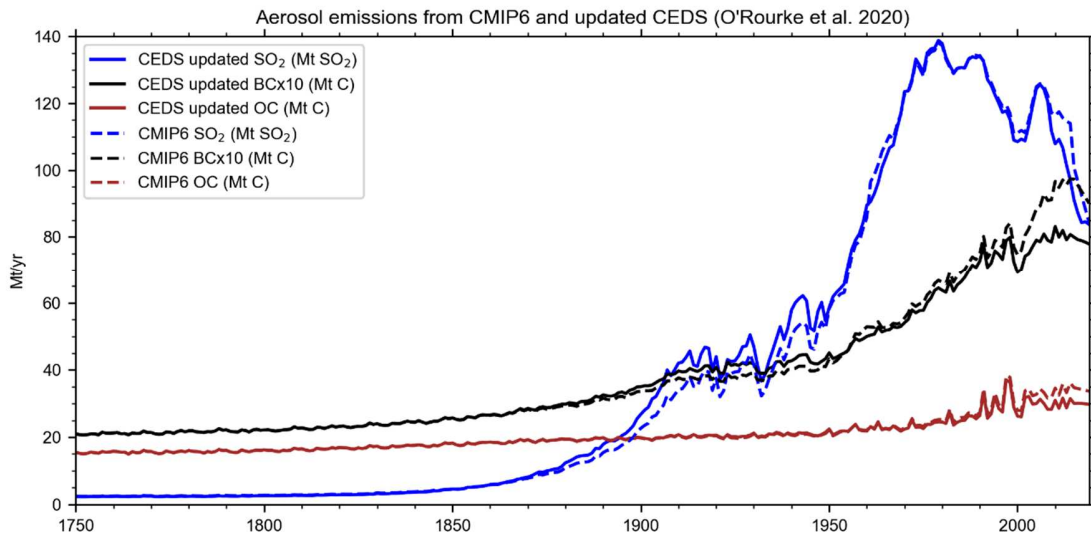


Figure S2: Comparison of the CMIP6 emissions dataset (dashed lines), used in running the CMIP6 models, with the updated CEDS emissions (O'Rourke et al., 2020) plus biomass burning emissions which are unchanged (solid lines) used for generating the CMIP6-constrained forcing time series.

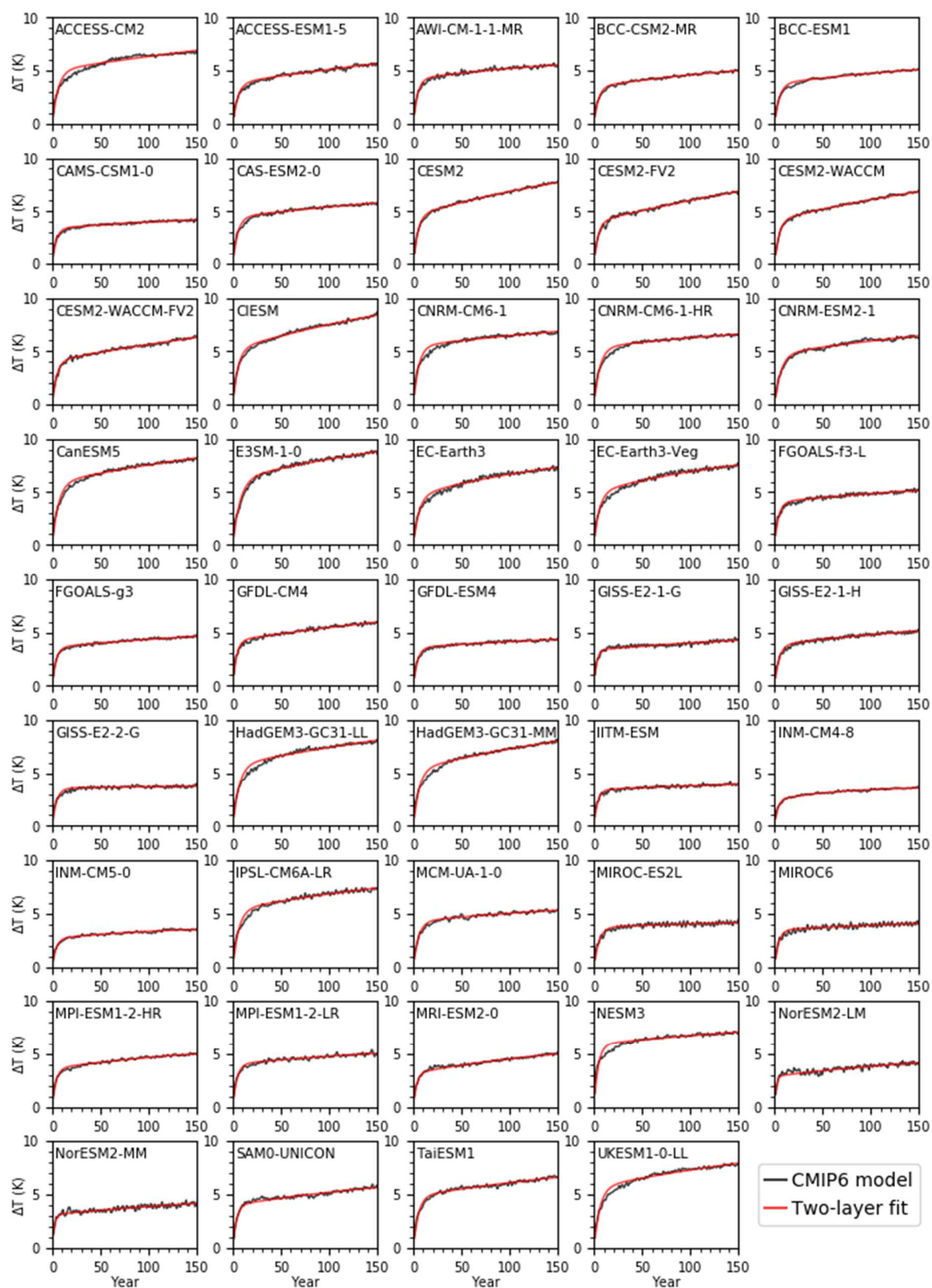


Figure S3: Two-layer model fits to CMIP6 abrupt 4xCO₂ global surface air temperature (GSAT).

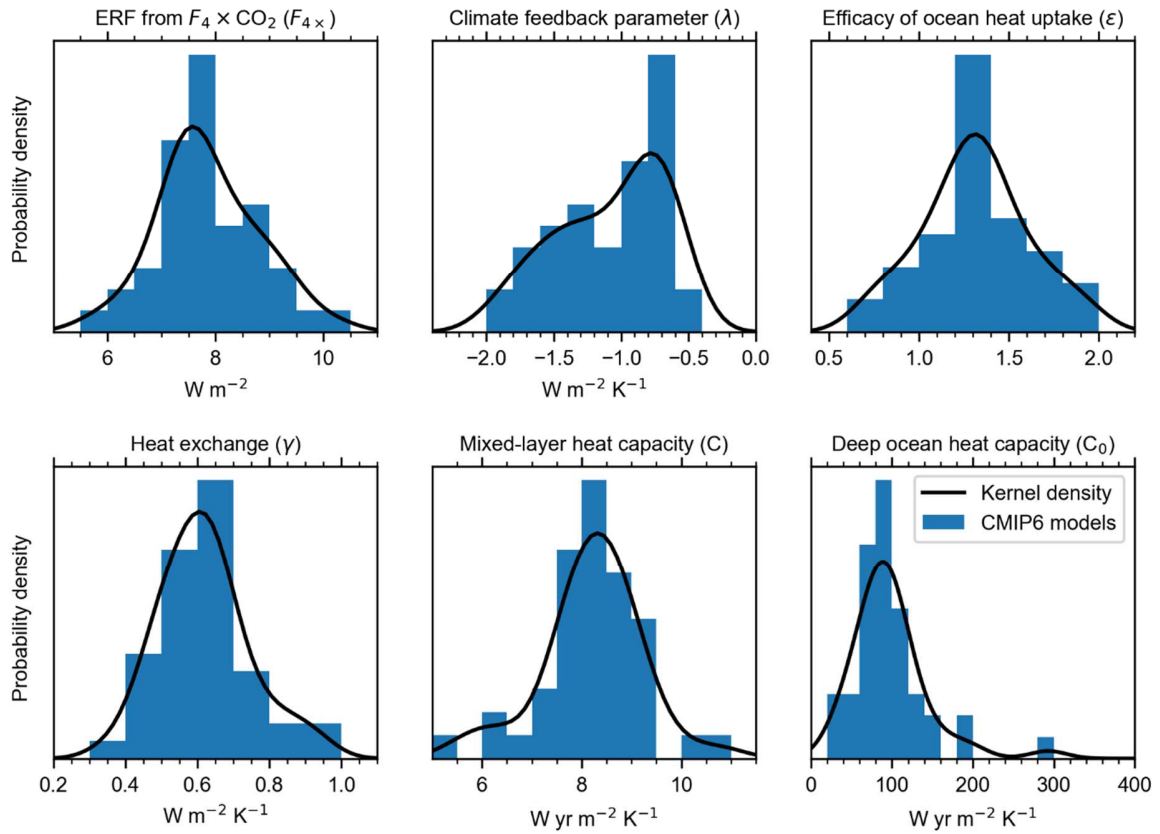


Figure S4: Histograms of Geoffroy model parameter emulations from CMIP6 model and kernel density estimate fit to distributions

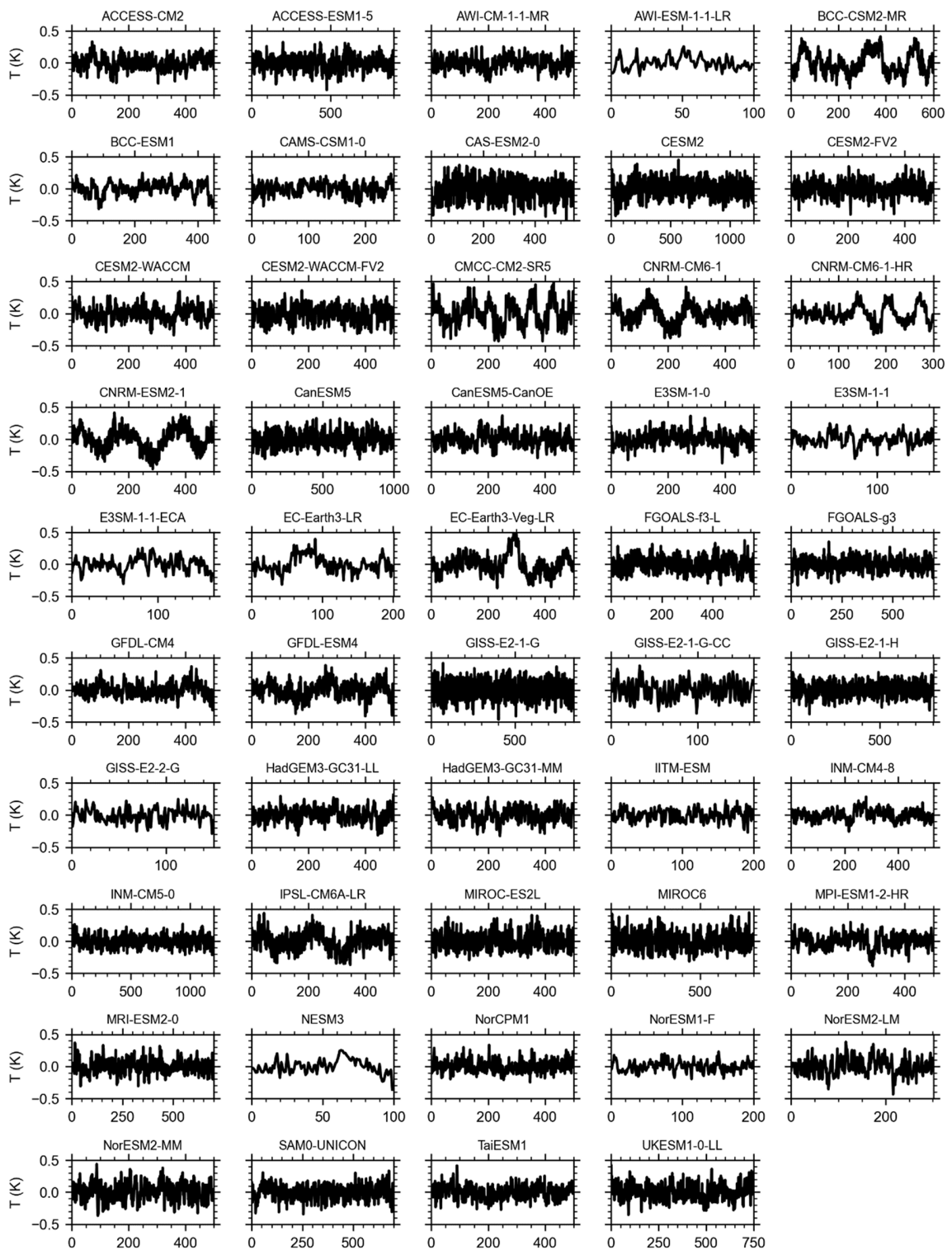


Figure S5: De-trended CMIP6 pre-industrial control global mean temperature anomalies used for characterisation of internal variability.

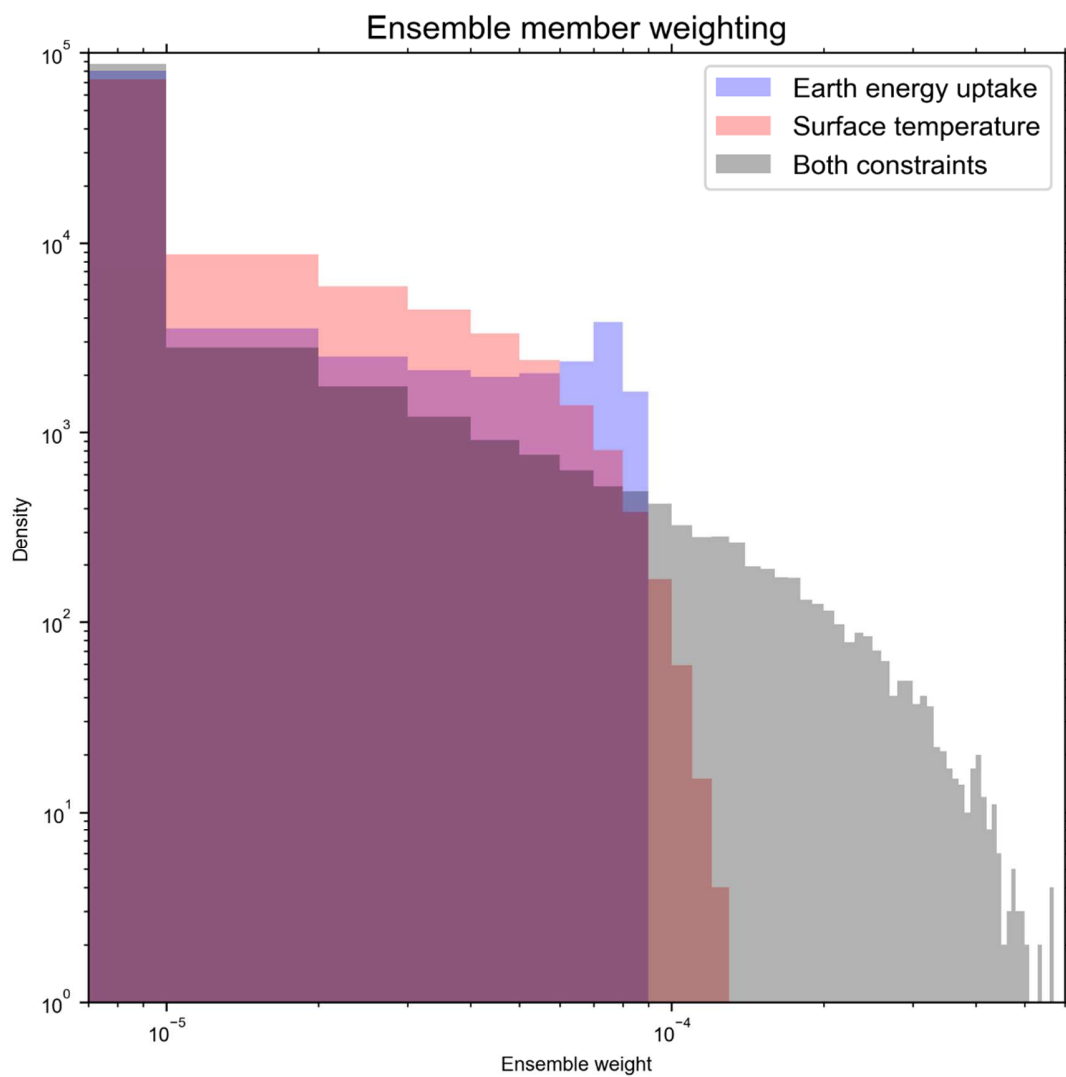


Figure S6: log-log histogram of ensemble member density using ocean heat uptake only (blue), surface temperature only (red) and both constraints (grey). Most ensemble members have a low weight and near-zero contribution to the total ensemble.

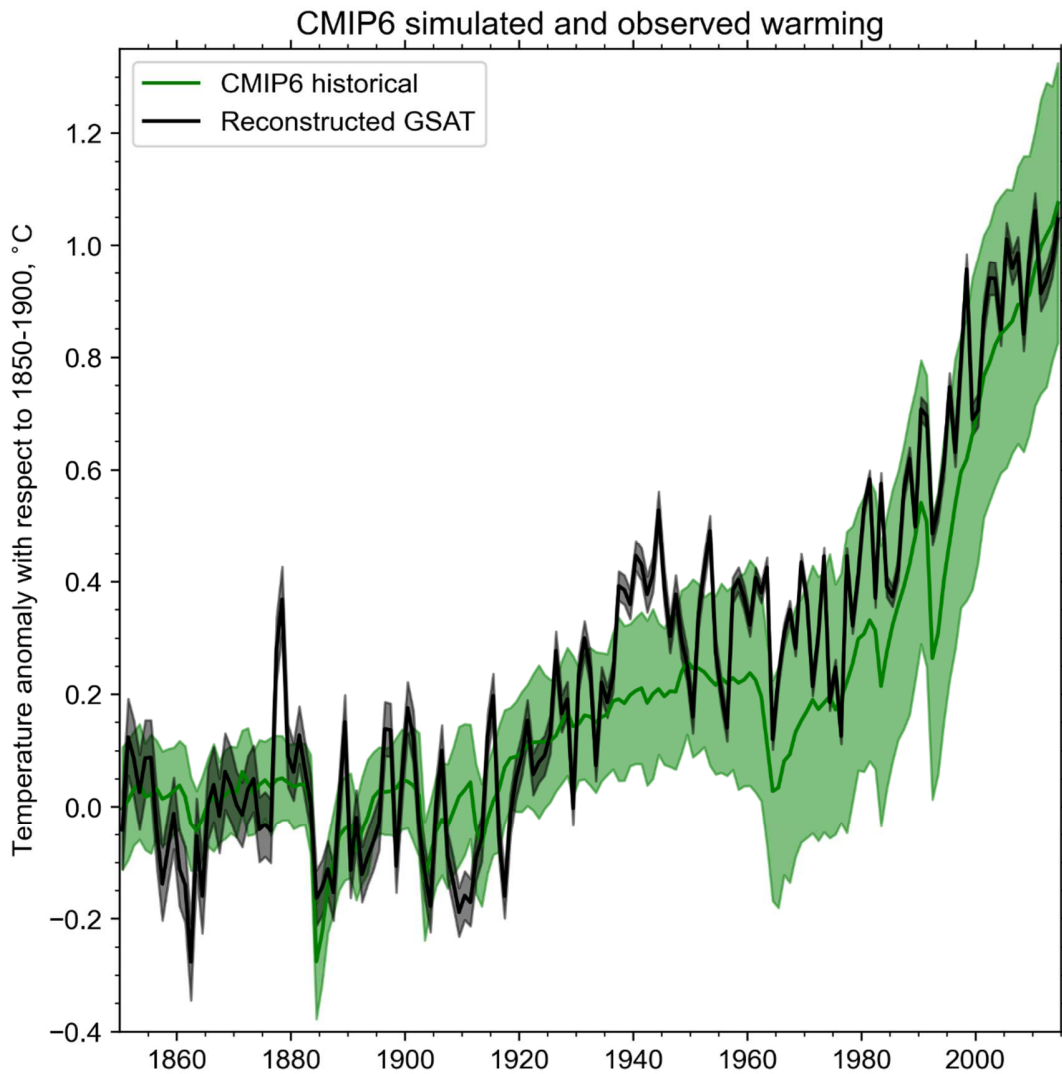


Figure S7: Historical warming simulated by 56 CMIP6 models compared with reconstructed GSAT observations. Anomalies expressed relative to 1850-1900. Models with multiple ensemble members are averaged, and each model contributed equal weight.

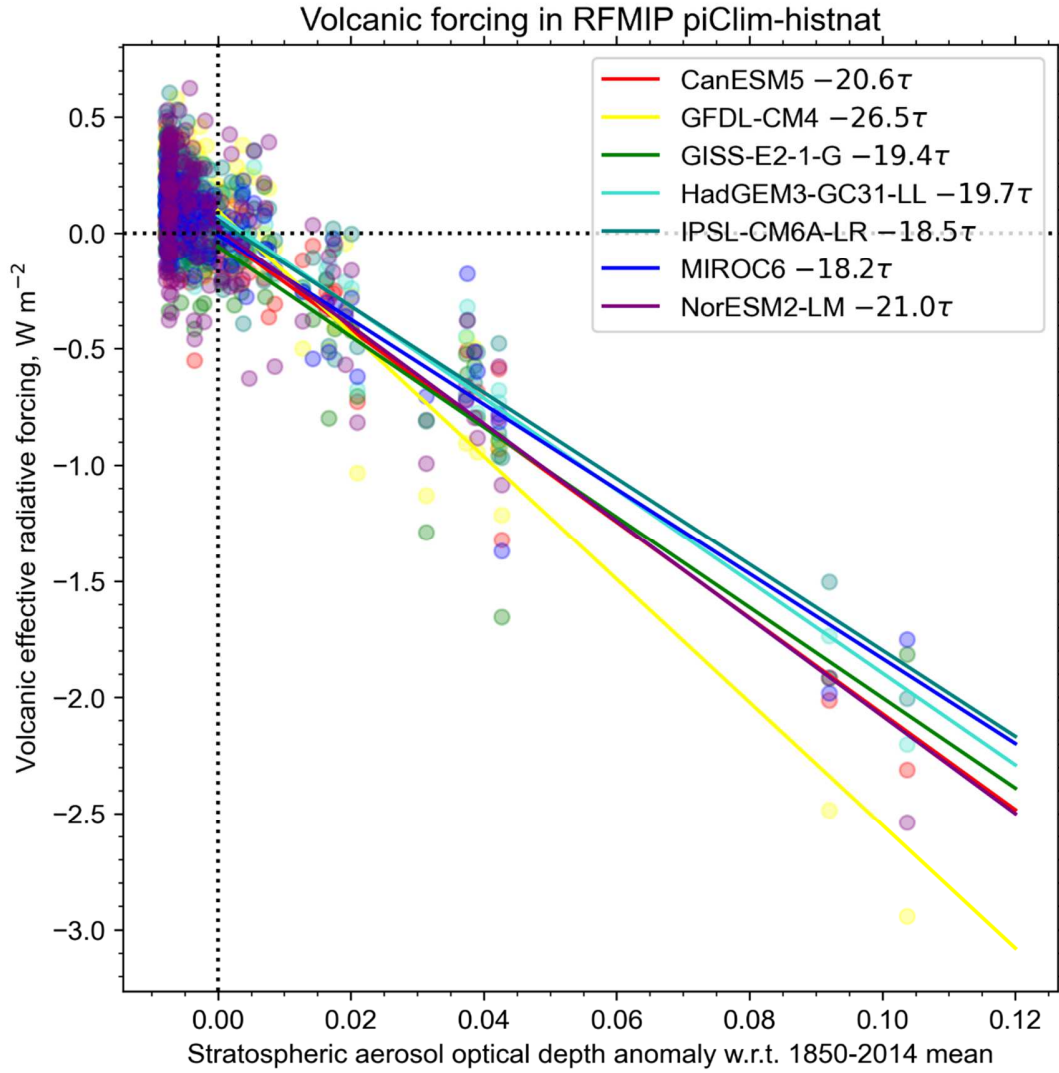


Figure S8: Regression plot of estimate of volcanic forcing from CMIP6 models (RFMIP histnat experiment minus time-varying best estimate of solar forcing, calculated as described in Text S1) against stratospheric aerosol optical depth.

Table S1: Two-layer model parameter fits for CMIP6 models.

Model	F_{4x}	λ	C_{mix}	C_{deep}	γ	ϵ	ECS
ACCESS-CM2	7.66	-0.69	8.82	97.46	0.53	1.49	5.57
ACCESS-ESM1-5	6.97	-0.72	9.02	96.79	0.61	1.71	4.83
AWI-CM-1-1-MR	8.41	-1.30	8.17	54.70	0.49	1.30	3.24
BCC-CSM2-MR	6.89	-1.06	8.51	73.69	0.64	1.32	3.25
BCC-ESM1	6.68	-0.94	8.47	91.72	0.58	1.33	3.57
CAMS-CSM1-0	8.88	-1.88	10.01	62.41	0.53	1.34	2.37
CAS-ESM2-0	7.13	-0.93	7.57	72.83	0.45	1.43	3.84
CESM2	8.84	-0.72	8.33	70.64	0.64	1.73	6.15

Model	F_{4x}	λ	C_{mix}	C_{deep}	γ	ε	ECS
CESM2-FV2	7.94	-0.56	7.96	91.10	0.70	1.91	7.10
CESM2-WACCM	8.28	-0.73	8.72	84.86	0.72	1.63	5.64
CESM2-WACCM-FV2	7.13	-0.59	7.60	111.71	0.71	1.54	6.00
CIESM	8.94	-0.72	8.59	73.23	0.67	1.38	6.25
CNRM-CM6-1	7.51	-0.77	7.05	121.14	0.56	1.03	4.88
CNRM-CM6-1-HR	7.53	-0.94	8.07	90.43	0.58	0.75	3.99
CNRM-ESM2-1	5.70	-0.63	7.48	94.94	0.61	0.87	4.51
CanESM5	7.61	-0.66	7.86	78.83	0.54	1.09	5.78
E3SM-1-0	7.42	-0.64	8.43	43.77	0.36	1.41	5.81
EC-Earth3	7.37	-0.82	8.46	38.41	0.48	1.43	4.48
EC-Earth3-Veg	7.81	-0.85	8.12	38.54	0.45	1.42	4.57
FGOALS-f3-L	9.54	-1.43	9.29	87.98	0.53	1.63	3.33
FGOALS-g3	7.87	-1.28	8.21	112.65	0.67	1.30	3.07
GFDL-CM4	8.45	-0.89	7.36	96.54	0.58	1.85	4.75
GFDL-ESM4	7.34	-1.27	8.44	129.94	0.60	1.23	2.88
GISS-E2-1-G	8.11	-1.46	6.52	145.03	0.85	1.09	2.78
GISS-E2-1-H	7.58	-1.17	8.76	83.36	0.63	1.21	3.25
GISS-E2-2-G	7.25	-1.63	8.63	293.05	0.57	0.72	2.23
HadGEM3-GC31-LL	7.46	-0.62	8.07	78.11	0.51	1.23	5.98
HadGEM3-GC31-MM	7.37	-0.67	7.85	70.75	0.61	1.07	5.53
IITM-ESM	9.25	-1.93	9.38	159.19	0.73	1.07	2.39
INM-CM4-8	6.25	-1.69	7.84	29.20	0.64	1.21	1.85
INM-CM5-0	6.35	-1.59	9.20	51.95	0.55	1.38	2.00
IPSL-CM6A-LR	7.52	-0.76	8.21	60.03	0.44	1.35	4.93
MCM-UA-1-0	7.12	-1.04	8.48	129.93	0.74	0.80	3.41
MIROC-ES2L	7.98	-1.54	10.82	199.60	0.66	0.89	2.59
MIROC6	7.73	-1.36	9.00	182.38	0.64	1.31	2.84
MPI-ESM1-2-HR	8.63	-1.34	8.89	84.13	0.66	1.49	3.23
MPI-ESM1-2-LR	9.28	-1.46	9.25	104.63	0.63	1.29	3.18
MRI-ESM2-0	8.03	-1.20	7.89	92.84	0.94	1.34	3.34
NESM3	7.72	-0.83	5.50	103.69	0.47	0.97	4.62
NorESM2-LM	10.21	-1.77	6.01	115.66	0.90	1.92	2.89
NorESM2-MM	9.39	-1.69	6.13	116.97	0.79	1.66	2.77
SAM0-UNICON	8.69	-1.14	7.67	106.86	0.82	1.21	3.83
TaiESM1	8.51	-0.92	8.72	97.26	0.63	1.27	4.64
UKESM1-0-LL	7.61	-0.68	7.77	77.15	0.54	1.14	5.57

Table S2: Correlation coefficients used for six-dimensional joint kernel density estimate for obtaining random “meta-models” derived from CMIP6 model fits.

	F_{4x}	λ	C	C_0	γ	ϵ
F_{4x}	1.0000	-0.4649	0.0134	0.0533	0.3159	0.4487
λ		1.0000	-0.3400	-0.3828	-0.1569	0.1990
C			1.0000	0.1686	-0.4411	-0.4355
C_0				1.0000	0.1046	-0.2542
γ					1.0000	0.2857
ϵ						1.0000

Table S3: 5th, 50th and 95th percentile aerosol forcing trend from 1980-2014 in CMIP6-constrained and 12 CMIP6/chemistry-transport models, in $W m^{-2} decade^{-1}$. Values plotted in Fig. 7.

Time series	5%	mean	95%
CMIP6-constrained	-0.074	0.025	0.111
Unconstrained	-0.086	0.088	0.282
CanESM5	0.042	0.065	0.089
E3SM-1-0	0.020	0.069	0.118
GFDL-CM4	0.040	0.078	0.115
GFDL-ESM4	-0.023	0.037	0.097
GISS-E2-1-G	-0.070	-0.026	0.018
HadGEM3-GC31-LL	0.037	0.066	0.094
IPSL-CM6A-LR	-0.078	-0.03	0.019
MIROC6	-0.040	-0.011	0.017
MRI-ESM2-0	-0.103	-0.024	0.056
NorESM2-LM	0.014	0.064	0.113
UKESM1-0-LL	0.081	0.152	0.222

Table S4: Mean, median, 68% and 90% ranges for aerosol forcing, ECS and TCR from each scaled historical aerosol time series based on weighted percentiles of the distribution after applying constraints. Aerosol ERFs are for 2019 relative to 1750. For CMIP6-constrained, aerosol forcing estimates are from the updated CEDS emissions (O’Rourke et al., 2020), whereas for CMIP6 model estimates they are from SSP2-4.5.

Time series	Variable	5%	16%	median	mean	84%	95%
CMIP6-constrained	ECS ($^{\circ}C$)	1.76	2.15	2.89	3.10	3.94	5.11
	TCR ($^{\circ}C$)	1.24	1.43	1.80	1.83	2.22	2.57
	ERFaer ($W m^{-2}$)	-1.55	-1.26	-0.87	-0.90	-0.54	-0.35
	ERFari ($W m^{-2}$)	-0.62	-0.47	-0.29	-0.31	-0.15	-0.08
	ERFaci ($W m^{-2}$)	-1.18	-0.93	-0.56	-0.59	-0.26	-0.10
CanESM5	ECS ($^{\circ}C$)	1.66	1.98	2.65	2.78	3.44	4.29
	TCR ($^{\circ}C$)	1.17	1.34	1.67	1.69	2.03	2.32
	ERFaer ($W m^{-2}$)	-0.97	-0.72	-0.36	-0.39	-0.08	0.08
	ERFari ($W m^{-2}$)	0.04	0.07	0.12	0.12	0.18	0.22
	ERFaci ($W m^{-2}$)	-1.05	-0.83	-0.48	-0.51	-0.22	-0.09
E3SM1-0	ECS ($^{\circ}C$)	1.81	2.21	2.95	3.18	4.07	5.32

Time series	Variable	5%	16%	median	mean	84%	95%
	TCR (°C)	1.26	1.47	1.81	1.86	2.24	2.59
	ERFaer (W m ⁻²)	-1.28	-1.10	-0.83	-0.83	-0.56	-0.40
	ERFari (W m ⁻²)	-0.60	-0.49	-0.33	-0.34	-0.20	-0.13
	ERFaci (W m ⁻²)	-0.91	-0.74	-0.48	-0.49	-0.24	-0.10
GFDL-CM4	ECS (°C)	1.75	2.13	2.85	3.03	3.80	4.88
	TCR (°C)	1.23	1.42	1.76	1.79	2.15	2.46
	ERFaer (W m ⁻²)	-1.08	-0.88	-0.58	-0.60	-0.33	-0.20
	ERFari (W m ⁻²)	-0.21	-0.17	-0.12	-0.12	-0.07	-0.04
	ERFaci (W m ⁻²)	-0.98	-0.77	-0.45	-0.48	-0.20	-0.06
GFDL-ESM4	ECS (°C)	1.78	2.17	2.88	3.10	3.91	5.15
	TCR (°C)	1.25	1.44	1.77	1.80	2.16	2.49
	ERFaer (W m ⁻²)	-1.23	-1.04	-0.73	-0.74	-0.45	-0.30
	ERFari (W m ⁻²)	-0.33	-0.27	-0.18	-0.19	-0.11	-0.07
	ERFaci (W m ⁻²)	-1.06	-0.86	-0.54	-0.56	-0.26	-0.11
GISS-E2-1-G	ECS (°C)	1.85	2.29	3.09	3.40	4.41	5.95
	TCR (°C)	1.29	1.50	1.87	1.93	2.35	2.75
	ERFaer (W m ⁻²)	-1.70	-1.43	-0.99	-1.00	-0.58	-0.35
	ERFari (W m ⁻²)	-0.26	-0.21	-0.15	-0.15	-0.09	-0.06
	ERFaci (W m ⁻²)	-1.57	-1.29	-0.84	-0.85	-0.43	-0.20
HadGEM3-GC31-LL	ECS (°C)	1.75	2.13	2.87	3.05	3.86	4.89
	TCR (°C)	1.23	1.42	1.77	1.81	2.18	2.50
	ERFaer (W m ⁻²)	-1.36	-1.14	-0.80	-0.81	-0.49	-0.31
	ERFari (W m ⁻²)	-0.37	-0.30	-0.20	-0.21	-0.12	-0.08
	ERFaci (W m ⁻²)	-1.17	-0.94	-0.58	-0.60	-0.27	-0.10
IPSL-CM6A-LR	ECS (°C)	1.80	2.22	2.98	3.21	4.14	5.42
	TCR (°C)	1.26	1.46	1.83	1.87	2.26	2.63
	ERFaer (W m ⁻²)	-1.25	-1.08	-0.82	-0.82	-0.55	-0.40
	ERFari (W m ⁻²)	-0.63	-0.51	-0.35	-0.36	-0.21	-0.13
	ERFaci (W m ⁻²)	-0.85	-0.70	-0.45	-0.46	-0.23	-0.10
MIROC6	ECS (°C)	1.88	2.32	3.11	3.44	4.46	6.03
	TCR (°C)	1.30	1.52	1.88	1.94	2.36	2.76
	ERFaer (W m ⁻²)	-1.62	-1.38	-0.99	-1.00	-0.61	-0.40
	ERFari (W m ⁻²)	-0.43	-0.35	-0.24	-0.25	-0.14	-0.09
	ERFaci (W m ⁻²)	-1.40	-1.14	-0.73	-0.75	-0.36	-0.16
MRI-ESM2-0	ECS (°C)	1.77	2.16	2.93	3.14	4.00	5.18
	TCR (°C)	1.24	1.44	1.80	1.84	2.23	2.58
	ERFaer (W m ⁻²)	-1.27	-1.09	-0.79	-0.80	-0.52	-0.36
	ERFari (W m ⁻²)	-0.52	-0.42	-0.29	-0.30	-0.17	-0.11
	ERFaci (W m ⁻²)	-0.97	-0.78	-0.49	-0.50	-0.23	-0.10
NorESM2-LM	ECS (°C)	1.76	2.15	2.89	3.09	3.92	5.07
	TCR (°C)	1.24	1.43	1.78	1.82	2.20	2.52
	ERFaer (W m ⁻²)	-0.87	-0.67	-0.37	-0.39	-0.12	0.02
	ERFari (W m ⁻²)	0.03	0.04	0.07	0.07	0.10	0.13
	ERFaci (W m ⁻²)	-0.92	-0.74	-0.44	-0.46	-0.20	-0.07

Time series	Variable	5%	16%	median	mean	84%	95%
Oslo-CTM3	ECS (°C)	1.80	2.22	3.00	3.26	4.17	5.59
	TCR (°C)	1.26	1.47	1.83	1.88	2.28	2.65
	ERFaer (W m ⁻²)	-1.42	-1.19	-0.83	-0.86	-0.52	-0.35
	ERFari (W m ⁻²)	-0.43	-0.35	-0.24	-0.25	-0.15	-0.09
	ERFaci (W m ⁻²)	-1.20	-0.95	-0.58	-0.61	-0.27	-0.10
UKESM1-0-LL	ECS (°C)	1.71	2.07	2.76	2.89	3.62	4.49
	TCR (°C)	1.21	1.39	1.73	1.75	2.10	2.39
	ERFaer (W m ⁻²)	-1.13	-0.96	-0.70	-0.71	-0.45	-0.31
	ERFari (W m ⁻²)	-0.47	-0.38	-0.26	-0.26	-0.15	-0.10
	ERFaci (W m ⁻²)	-0.86	-0.69	-0.42	-0.44	-0.20	-0.07

Table S5: As Table S4, using only global-mean surface air temperature as the constraint.

Time series	Variable	5%	16%	median	mean	84%	95%
CMIP6-constrained	ECS (°C)	1.93	2.34	3.08	3.39	4.36	5.84
	TCR (°C)	1.33	1.53	1.84	1.89	2.25	2.60
	ERFaer (W m ⁻²)	-1.43	-1.14	-0.77	-0.80	-0.45	-0.28
	ERFari (W m ⁻²)	-0.59	-0.44	-0.27	-0.29	-0.13	-0.06
	ERFaci (W m ⁻²)	-1.08	-0.82	-0.48	-0.51	-0.21	-0.05
CanESM5	ECS (°C)	1.89	2.29	2.96	3.22	4.06	5.35
	TCR (°C)	1.31	1.50	1.79	1.82	2.15	2.44
	ERFaer (W m ⁻²)	-0.83	-0.59	-0.25	-0.29	0.00	0.14
	ERFari (W m ⁻²)	0.05	0.07	0.13	0.13	0.18	0.22
	ERFaci (W m ⁻²)	-0.93	-0.70	-0.38	-0.42	-0.15	-0.02
E3SM1-0	ECS (°C)	1.92	2.33	3.06	3.38	4.33	5.84
	TCR (°C)	1.33	1.53	1.84	1.89	2.25	2.60
	ERFaer (W m ⁻²)	-1.22	-1.04	-0.76	-0.77	-0.49	-0.34
	ERFari (W m ⁻²)	-0.57	-0.46	-0.31	-0.33	-0.19	-0.12
	ERFaci (W m ⁻²)	-0.87	-0.69	-0.43	-0.44	-0.19	-0.07
GFDL-CM4	ECS (°C)	1.92	2.33	3.04	3.33	4.26	5.65
	TCR (°C)	1.33	1.53	1.82	1.87	2.21	2.52
	ERFaer (W m ⁻²)	-1.01	-0.80	-0.52	-0.54	-0.28	-0.15
	ERFari (W m ⁻²)	-0.20	-0.16	-0.11	-0.12	-0.07	-0.04
	ERFaci (W m ⁻²)	-0.91	-0.69	-0.40	-0.42	-0.15	-0.02
GFDL-ESM4	ECS (°C)	1.89	2.28	2.96	3.22	4.07	5.41
	TCR (°C)	1.31	1.50	1.79	1.83	2.16	2.47
	ERFaer (W m ⁻²)	-1.17	-0.96	-0.64	-0.66	-0.38	-0.23
	ERFari (W m ⁻²)	-0.32	-0.26	-0.18	-0.18	-0.10	-0.07
	ERFaci (W m ⁻²)	-1.00	-0.78	-0.45	-0.48	-0.19	-0.06
GISS-E2-1-G	ECS (°C)	1.95	2.37	3.15	3.51	4.56	6.24
	TCR (°C)	1.34	1.55	1.88	1.94	2.33	2.72
	ERFaer (W m ⁻²)	-1.62	-1.32	-0.87	-0.89	-0.47	-0.26
	ERFari (W m ⁻²)	-0.26	-0.21	-0.14	-0.15	-0.08	-0.05
	ERFaci (W m ⁻²)	-1.49	-1.18	-0.72	-0.75	-0.32	-0.12
HadGEM3-	ECS (°C)	1.93	2.34	3.07	3.37	4.32	5.78

Time series	Variable	5%	16%	median	mean	84%	95%
GC31-LL	TCR (°C)	1.33	1.53	1.84	1.88	2.24	2.57
	ERFaer (W m ⁻²)	-1.29	-1.07	-0.73	-0.75	-0.43	-0.27
	ERFari (W m ⁻²)	-0.36	-0.29	-0.20	-0.20	-0.12	-0.07
	ERFaci (W m ⁻²)	-1.10	-0.87	-0.52	-0.55	-0.23	-0.06
IPSL-CM6A-LR	ECS (°C)	1.94	2.35	3.12	3.45	4.46	6.04
	TCR (°C)	1.34	1.54	1.86	1.92	2.30	2.67
	ERFaer (W m ⁻²)	-1.20	-1.03	-0.76	-0.76	-0.50	-0.35
	ERFari (W m ⁻²)	-0.60	-0.48	-0.32	-0.34	-0.19	-0.12
	ERFaci (W m ⁻²)	-0.81	-0.66	-0.41	-0.42	-0.20	-0.08
MIROC6	ECS (°C)	1.95	2.38	3.17	3.53	4.58	6.27
	TCR (°C)	1.35	1.56	1.88	1.94	2.34	2.72
	ERFaer (W m ⁻²)	-1.56	-1.29	-0.88	-0.90	-0.52	-0.32
	ERFari (W m ⁻²)	-0.42	-0.34	-0.23	-0.24	-0.14	-0.09
	ERFaci (W m ⁻²)	-1.34	-1.05	-0.63	-0.66	-0.28	-0.09
MRI-ESM2-0	ECS (°C)	1.93	2.34	3.08	3.39	4.35	5.82
	TCR (°C)	1.33	1.54	1.85	1.89	2.25	2.60
	ERFaer (W m ⁻²)	-1.20	-1.01	-0.71	-0.73	-0.45	-0.31
	ERFari (W m ⁻²)	-0.51	-0.41	-0.28	-0.29	-0.17	-0.11
	ERFaci (W m ⁻²)	-0.90	-0.70	-0.42	-0.44	-0.18	-0.06
NorESM2-LM	ECS (°C)	1.93	2.34	3.07	3.38	4.33	5.79
	TCR (°C)	1.33	1.53	1.84	1.88	2.24	2.57
	ERFaer (W m ⁻²)	-0.79	-0.59	-0.31	-0.33	-0.08	0.05
	ERFari (W m ⁻²)	0.03	0.04	0.07	0.07	0.10	0.13
	ERFaci (W m ⁻²)	-0.85	-0.66	-0.38	-0.40	-0.16	-0.03
Oslo-CTM3	ECS (°C)	1.95	2.37	3.15	3.49	4.51	6.13
	TCR (°C)	1.34	1.55	1.87	1.92	2.30	2.66
	ERFaer (W m ⁻²)	-1.34	-1.09	-0.74	-0.77	-0.45	-0.29
	ERFari (W m ⁻²)	-0.43	-0.35	-0.24	-0.25	-0.14	-0.09
	ERFaci (W m ⁻²)	-1.11	-0.86	-0.49	-0.52	-0.20	-0.05
UKESM1-0-LL	ECS (°C)	1.90	2.31	3.00	3.27	4.15	5.47
	TCR (°C)	1.32	1.52	1.81	1.85	2.18	2.49
	ERFaer (W m ⁻²)	-1.07	-0.91	-0.65	-0.66	-0.41	-0.28
	ERFari (W m ⁻²)	-0.44	-0.36	-0.24	-0.25	-0.14	-0.09
	ERFaci (W m ⁻²)	-0.82	-0.65	-0.39	-0.41	-0.17	-0.05

Table S6: As Table S4, using only Earth energy uptake as the constraint.

Time series	Variable	5%	16%	median	mean	84%	95%
CMIP6-constrained	ECS (°C)	1.95	2.38	3.26	3.75	4.98	7.12
	TCR (°C)	1.33	1.54	1.94	2.05	2.55	3.13
	ERFaer (W m ⁻²)	-1.83	-1.53	-1.09	-1.10	-0.66	-0.39
	ERFari (W m ⁻²)	-0.64	-0.47	-0.29	-0.30	-0.14	-0.02
	ERFaci (W m ⁻²)	-1.48	-1.20	-0.78	-0.80	-0.39	-0.18
CanESM5	ECS (°C)	1.90	2.33	3.20	3.68	4.89	7.00

Time series	Variable	5%	16%	median	mean	84%	95%
	TCR (°C)	1.31	1.52	1.91	2.02	2.51	3.09
	ERFaer (W m ⁻²)	-1.22	-0.96	-0.56	-0.57	-0.18	0.04
	ERFari (W m ⁻²)	0.08	0.13	0.21	0.21	0.30	0.36
	ERFaci (W m ⁻²)	-1.40	-1.15	-0.77	-0.78	-0.40	-0.20
E3SM1-0	ECS (°C)	1.96	2.38	3.25	3.73	4.95	7.03
	TCR (°C)	1.33	1.54	1.94	2.04	2.54	3.11
	ERFaer (W m ⁻²)	-1.52	-1.32	-0.99	-0.99	-0.65	-0.46
	ERFari (W m ⁻²)	-0.63	-0.52	-0.36	-0.37	-0.22	-0.14
	ERFaci (W m ⁻²)	-1.15	-0.94	-0.62	-0.62	-0.30	-0.14
GFDL-CM4	ECS (°C)	1.99	2.41	3.30	3.80	5.10	7.23
	TCR (°C)	1.35	1.56	1.95	2.07	2.57	3.16
	ERFaer (W m ⁻²)	-1.40	-1.18	-0.83	-0.84	-0.49	-0.30
	ERFari (W m ⁻²)	-0.25	-0.21	-0.14	-0.15	-0.09	-0.06
	ERFaci (W m ⁻²)	-1.27	-1.04	-0.67	-0.69	-0.33	-0.15
GFDL-ESM4	ECS (°C)	1.96	2.39	3.27	3.76	5.01	7.13
	TCR (°C)	1.33	1.54	1.94	2.05	2.55	3.14
	ERFaer (W m ⁻²)	-1.46	-1.26	-0.93	-0.92	-0.58	-0.39
	ERFari (W m ⁻²)	-0.41	-0.33	-0.23	-0.24	-0.14	-0.09
	ERFaci (W m ⁻²)	-1.23	-1.02	-0.68	-0.69	-0.35	-0.17
GISS-E2-1-G	ECS (°C)	1.97	2.39	3.26	3.75	4.98	7.09
	TCR (°C)	1.33	1.54	1.94	2.05	2.55	3.13
	ERFaer (W m ⁻²)	-1.93	-1.62	-1.14	-1.14	-0.65	-0.39
	ERFari (W m ⁻²)	-0.27	-0.22	-0.15	-0.16	-0.09	-0.06
	ERFaci (W m ⁻²)	-1.78	-1.47	-0.98	-0.98	-0.49	-0.24
HadGEM3-GC31-LL	ECS (°C)	1.96	2.38	3.27	3.75	4.98	7.07
	TCR (°C)	1.33	1.54	1.94	2.05	2.55	3.12
	ERFaer (W m ⁻²)	-1.85	-1.57	-1.13	-1.13	-0.68	-0.43
	ERFari (W m ⁻²)	-0.41	-0.33	-0.23	-0.24	-0.14	-0.09
	ERFaci (W m ⁻²)	-1.63	-1.34	-0.89	-0.89	-0.44	-0.20
IPSL-CM6A-LR	ECS (°C)	1.97	2.39	3.27	3.75	4.99	7.07
	TCR (°C)	1.34	1.54	1.94	2.05	2.55	3.13
	ERFaer (W m ⁻²)	-1.54	-1.34	-1.01	-1.00	-0.66	-0.46
	ERFari (W m ⁻²)	-0.62	-0.51	-0.35	-0.36	-0.21	-0.14
	ERFaci (W m ⁻²)	-1.16	-0.96	-0.64	-0.64	-0.32	-0.15
MIROC6	ECS (°C)	1.98	2.41	3.29	3.78	5.03	7.13
	TCR (°C)	1.34	1.55	1.95	2.06	2.56	3.14
	ERFaer (W m ⁻²)	-1.81	-1.54	-1.11	-1.11	-0.68	-0.44
	ERFari (W m ⁻²)	-0.45	-0.37	-0.25	-0.26	-0.15	-0.10
	ERFaci (W m ⁻²)	-1.56	-1.28	-0.84	-0.85	-0.41	-0.19
MRI-ESM2-0	ECS (°C)	1.93	2.35	3.19	3.66	4.86	6.93
	TCR (°C)	1.32	1.52	1.92	2.03	2.53	3.10
	ERFaer (W m ⁻²)	-1.56	-1.36	-1.00	-1.00	-0.63	-0.42
	ERFari (W m ⁻²)	-0.54	-0.45	-0.31	-0.32	-0.19	-0.12
	ERFaci (W m ⁻²)	-1.24	-1.02	-0.67	-0.68	-0.32	-0.15

Time series	Variable	5%	16%	median	mean	84%	95%
NorESM2-LM	ECS (°C)	1.97	2.39	3.28	3.76	5.01	7.11
	TCR (°C)	1.34	1.55	1.94	2.05	2.56	3.13
	ERFaer (W m ⁻²)	-1.10	-0.89	-0.55	-0.56	-0.22	-0.05
	ERFari (W m ⁻²)	0.03	0.05	0.08	0.09	0.12	0.15
	ERFaci (W m ⁻²)	-1.18	-0.97	-0.63	-0.64	-0.31	-0.14
Oslo-CTM3	ECS (°C)	1.97	2.39	3.28	3.77	5.02	7.14
	TCR (°C)	1.34	1.55	1.94	2.05	2.56	3.13
	ERFaer (W m ⁻²)	-1.68	-1.43	-1.04	-1.04	-0.65	-0.43
	ERFari (W m ⁻²)	-0.50	-0.41	-0.28	-0.29	-0.17	-0.11
	ERFaci (W m ⁻²)	-1.40	-1.14	-0.74	-0.75	-0.36	-0.16
UKESM1-0-LL	ECS (°C)	1.93	2.35	3.23	3.70	4.90	6.97
	TCR (°C)	1.32	1.53	1.93	2.03	2.53	3.10
	ERFaer (W m ⁻²)	-1.63	-1.40	-1.03	-1.03	-0.65	-0.43
	ERFari (W m ⁻²)	-0.50	-0.41	-0.29	-0.29	-0.18	-0.11
	ERFaci (W m ⁻²)	-1.35	-1.11	-0.73	-0.73	-0.35	-0.16

References

- Bond, T. C., Doherty, S. J., Fahey, D. W., Forster, P. M., Berntsen, T., Deangelo, B. J., et al. (2013). Bounding the role of black carbon in the climate system: A scientific assessment. *Journal of Geophysical Research Atmospheres*, *118*(11), 5380–5552. <https://doi.org/10.1002/jgrd.50171>
- Etminan, M., Myhre, G., Highwood, E. J., & Shine, K. P. (2016). Radiative forcing of carbon dioxide, methane, and nitrous oxide: A significant revision of the methane radiative forcing. *Geophysical Research Letters*, *43*(24), 12,614–12,623. <https://doi.org/10.1002/2016GL071930>
- Ghimire, B., Williams, C. A., Masek, J., Gao, F., Wang, Z., Schaaf, C., & He, T. (2014). Global albedo change and radiative cooling from anthropogenic land cover change, 1700 to 2005 based on MODIS, land use harmonization, radiative kernels, and reanalysis. *Geophysical Research Letters*, *41*(24), 9087–9096. <https://doi.org/10.1002/2014GL061671>
- Gidden, M. J., Riahi, K., Smith, S. J., Fujimori, S., Luderer, G., Kriegler, E., et al. (2019). Global emissions pathways under different socioeconomic scenarios for use in CMIP6: a dataset of harmonized emissions trajectories through the end of the century. *Geoscientific Model Development*, *12*(4), 1443–1475. <https://doi.org/10.5194/gmd-12-1443-2019>
- Global Volcanism Program. (2013). Volcanoes of the World v.4.9.0. Smithsonian Institution. <https://doi.org/10.5479/si.GVP.VOTW4-2013>
- Gray, L. J., Rumbold, S. T., & Shine, K. P. (2009). Stratospheric Temperature and Radiative Forcing Response to 11-Year Solar Cycle Changes in Irradiance and Ozone. *Journal of the Atmospheric Sciences*, *66*(8), 2402–2417. <https://doi.org/10.1175/2009JAS2866.1>
- Hodnebrog, Ø., Myhre, G., Kramer, R. J., Shine, K. P., Andrews, T., Faluvegi, G., et al. (2020). The effect of rapid adjustments to halocarbons and N₂O on radiative

- forcing. *Npj Climate and Atmospheric Science*, 3(1). <https://doi.org/10.1038/s41612-020-00150-x>
- Hodnebrog, Ø., Aamaas, B., Fuglestedt, J. S., Marston, G., Myhre, G., Nielsen, C. J., et al. (2020). Updated Global Warming Potentials and Radiative Efficiencies of Halocarbons and Other Weak Atmospheric Absorbers. *Reviews of Geophysics*, 58(3). <https://doi.org/10.1029/2019RG000691>
- Kovilakam, M., Thomason, L. W., Ernest, N., Rieger, L., Bourassa, A., & Millán, L. (2020). The Global Space-based Stratospheric Aerosol Climatology (version 2.0): 1979–2018. *Earth System Science Data*, 12(4), 2607–2634. <https://doi.org/10.5194/essd-12-2607-2020>
- Larson, E. J. L., & Portmann, R. W. (2016). A temporal kernel method to compute effective radiative forcing in CMIP5 transient simulations. *Journal of Climate*, 29(4), 1497–1509. <https://doi.org/10.1175/JCLI-D-15-0577.1>
- Lee, D. S., Fahey, D. W., Skowron, A., Allen, M. R., Burkhardt, U., Chen, Q., et al. (2020). The contribution of global aviation to anthropogenic climate forcing for 2000 to 2018. *Atmospheric Environment*, 244, 117834. <https://doi.org/10.1016/j.atmosenv.2020.117834>
- Matthes, K., Funke, B., Andersson, M. E., Barnard, L., Beer, J., Charbonneau, P., et al. (2017). Solar forcing for CMIP6 (v3.2). *Geoscientific Model Development*, 10(6), 2247–2302. <https://doi.org/10.5194/gmd-10-2247-2017>
- Meinshausen, M., Vogel, E., Nauels, A., Lorbacher, K., Meinshausen, N., Etheridge, D. M., et al. (2017). Historical greenhouse gas concentrations for climate modelling (CMIP6). *Geoscientific Model Development*, 10(5), 2057–2116. <https://doi.org/10.5194/gmd-10-2057-2017>
- Meinshausen, M., Nicholls, Z. R. J., Lewis, J., Gidden, M. J., Vogel, E., Freund, M., et al. (2020). The shared socio-economic pathway (SSP) greenhouse gas concentrations and their extensions to 2500. *Geoscientific Model Development*, 13(8), 3571–3605. <https://doi.org/10.5194/gmd-13-3571-2020>
- Myhre, G., Shindell, D., Bréon, F.-M., Collins, W., Fuglestedt, J., Huang, J., et al. (2013a). Anthropogenic and natural radiative forcing. In T. F. Stocker, D. Qin, G.-K. Plattner, M. Tignor, S. K. Allen, J. Boschung, et al. (Eds.), *Climate Change 2013 the Physical Science Basis: Working Group I Contribution to the Fifth Assessment Report of the Intergovernmental Panel on Climate Change* (Vol. 9781107057, pp. 659–740). Cambridge, United Kingdom and New York, NY, USA: Cambridge University Press. <https://doi.org/10.1017/CBO9781107415324.018>
- Myhre, G., Shindell, D., Bréon, F.-M., Collins, W., Fuglestedt, J., Huang, J., et al. (2013b). Anthropogenic and Natural Radiative Forcing. In Intergovernmental Panel on Climate Change (Ed.), *Climate Change 2013 - The Physical Science Basis* (pp. 659–740). Cambridge: Cambridge University Press. <https://doi.org/10.1017/CBO9781107415324.018>
- O'Rourke, P. R., Smith, S. J., McDuffie, E. E., Klimont, Z., Crippa, M., Mott, A., et al. (2020, September). CEDS v_2020_09_11 Pre-Release Emission Data. Zenodo. <https://doi.org/10.5281/zenodo.4025316>
- Sherwood, S., Dixit, V., & Salomez, C. (2018). The global warming potential of near-surface emitted water vapour. *Environmental Research Letters*, 13(10). <https://doi.org/10.1088/1748-9326/aae018>

- Skeie, R. B., Myhre, G., Hodnebrog, Ø., Cameron-Smith, P. J., Deushi, M., Hegglin, M. I., et al. (2020). Historical total ozone radiative forcing derived from CMIP6 simulations. *Npj Climate and Atmospheric Science*, 3(1).
<https://doi.org/10.1038/s41612-020-00131-0>
- Smith, C. J., Forster, P. M., Allen, M., Leach, N., Millar, R. J., Passerello, G. A., & Regayre, L. A. (2018). FAIR v1.3: a simple emissions-based impulse response and carbon cycle model. *Geoscientific Model Development*, 11(6), 2273–2297.
<https://doi.org/10.5194/gmd-11-2273-2018>
- Smith, C. J., Kramer, R. J., Myhre, G., Forster, P. M., Soden, B. J., Andrews, T., et al. (2018). Understanding Rapid Adjustments to Diverse Forcing Agents. *Geophysical Research Letters*, 45(21), 12,023–12,031. <https://doi.org/10.1029/2018GL079826>
- Smith, C. J., Kramer, R. J., Myhre, G., Alterskjær, K., Collins, W., Sima, A., et al. (2020). Effective radiative forcing and adjustments in CMIP6 models. *Atmospheric Chemistry and Physics*, 20(16), 9591–9618. <https://doi.org/10.5194/acp-20-9591-2020>
- Stevenson, D. S., Young, P. J., Naik, V., Lamarque, J.-F., Shindell, D. T., Voulgarakis, A., et al. (2013). Tropospheric ozone changes, radiative forcing and attribution to emissions in the Atmospheric Chemistry and Climate Model Intercomparison Project (ACCMIP). *Atmospheric Chemistry and Physics*, 13(6), 3063–3085.
<https://doi.org/10.5194/acp-13-3063-2013>
- Toohey, M., & Sigl, M. (2017). Volcanic stratospheric sulfur injections and aerosol optical depth from 500 BCE to 1900 CE. *Earth System Science Data*, 9(2), 809–831.
<https://doi.org/10.5194/essd-9-809-2017>
- Vieira, L. E. A., Solanki, S. K., Krivova, N. A., & Usoskin, I. (2011). Evolution of the solar irradiance during the Holocene. *Astronomy & Astrophysics*, 531, A6.
<https://doi.org/10.1051/0004-6361/201015843>